Cancer Cell

Article

Intratumoral immune triads are required for immunotherapy-mediated elimination of solid tumors

Graphical abstract

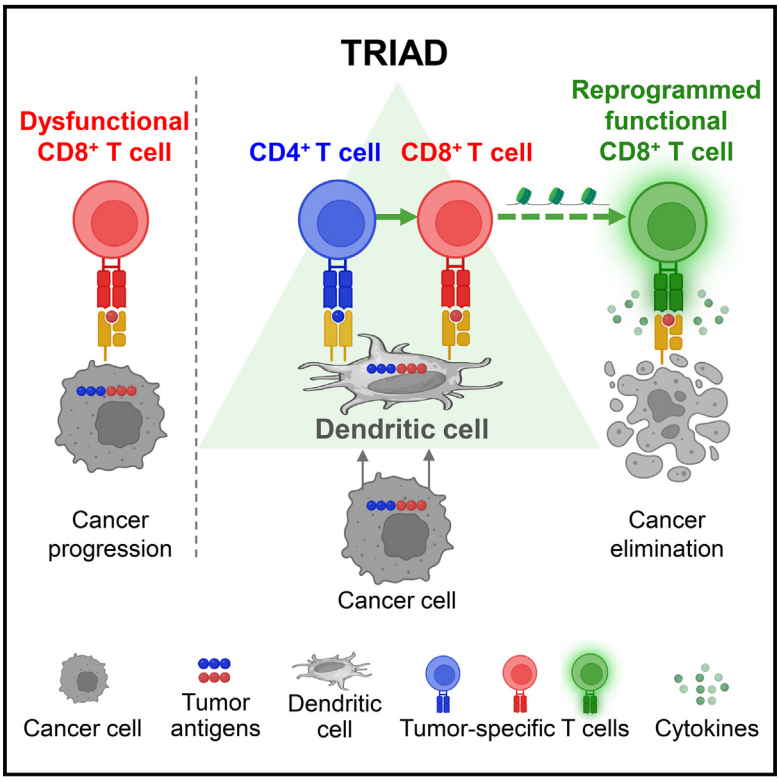

Highlights

- Intratumoral immune triads are required for cancer elimination
- CD4+ T cells within triads reprogram CD8+ T cells and license them to kill
- CD4+ T cells must engage with CD8+ T cells on same antigen-presenting cell
- Triads are associated with clinical responses to immunotherapy in humans

Authors

Gabriel Espinosa-Carrasco, Edison Chiu, Aurora Scrivo, ..., Bryan M. Burt, Hyun-Sung Lee, Andrea Schietinger

Correspondence

gespinosa@idibell.cat (G.E.-C.), schietia@mskcc.org (A.S.)

In brief

Tumor-specific CD8+ T cells are dysfunctional within tumors. Espinosa-Carrasco et al. show that CD4+ T cells must engage with CD8+ T cells on the same antigen-presenting cell (APC) during the effector phase, forming a three-cell-cluster (triad) to license CD8+ T cell cytotoxicity and CD8+ T cell-mediated cancer cell elimination.

Espinosa-Carrasco et al., 2024, Cancer Cell *42*, 1202–1216
July 8, 2024
https://doi.org/10.1016/j.ccell.2024.05.025

CellPress

CellPress

Cancer Cell

Article

Intratumoral immune triads are required for immunotherapy-mediated elimination of solid tumors

Gabriel Espinosa-Carrasco,[1,*] Edison Chiu,[1] Aurora Scrivo,[2] Paul Zumbo,[3,4] Asim Dave,[1] Doron Betel,[4,5,6] Sung Wook Kang,[7] Hee-Jin Jang,[7] Matthew D. Hellmann,[8,9] Bryan M. Burt,[7,10] Hyun-Sung Lee,[7] and Andrea Schietinger[1,11,12,*]

[1]Immunology Program, Memorial Sloan Kettering Cancer Center, New York, NY, USA
[2]Department of Developmental and Molecular Biology, and Institute for Aging Studies, Albert Einstein College of Medicine, Bronx, NY, USA
[3]Department of Physiology and Biophysics, Weill Cornell Medicine, New York, NY, USA
[4]Applied Bioinformatics Core, Weill Cornell Medicine, New York, NY, USA
[5]Institute for Computational Biomedicine, Weill Cornell Medicine, New York, NY, USA
[6]Division of Hematology and Medical Oncology, Department of Medicine, Weill Cornell Medicine, New York, NY, USA
[7]Systems Onco-Immunology Laboratory, David J. Sugarbaker Division of Thoracic Surgery, Michael E. DeBakey Department of Surgery, Baylor College of Medicine, Houston, TX, USA
[8]Oncology Service, Memorial Sloan Kettering Cancer Center, New York, NY, USA
[9]Department of Medicine, Weill Cornell Medicine, New York, NY, USA
[10]Division of Thoracic Surgery, University of California Los Angeles, Los Angeles, CA, USA
[11]Immunology and Microbial Pathogenesis Program, Weill Cornell Graduate School of Medical Sciences, New York, NY, USA
[12]Lead contact
*Correspondence: gespinosa@idibell.cat (G.E.-C.), schietia@mskcc.org (A.S.)
https://doi.org/10.1016/j.ccell.2024.05.025

SUMMARY

Tumor-specific CD8$^+$ T cells are frequently dysfunctional and unable to halt tumor growth. We investigated whether tumor-specific CD4$^+$ T cells can be enlisted to overcome CD8$^+$ T cell dysfunction within tumors. We find that the spatial positioning and interactions of CD8$^+$ and CD4$^+$ T cells, but not their numbers, dictate anti-tumor responses in the context of adoptive T cell therapy as well as immune checkpoint blockade (ICB): CD4$^+$ T cells must engage with CD8$^+$ T cells on the same dendritic cell during the effector phase, forming a three-cell-type cluster (triad) to license CD8$^+$ T cell cytotoxicity and cancer cell elimination. When intratumoral triad formation is disrupted, tumors progress despite equal numbers of tumor-specific CD8$^+$ and CD4$^+$ T cells. In patients with pleural mesothelioma treated with ICB, triads are associated with clinical responses. Thus, CD4$^+$ T cells and triads are required for CD8$^+$ T cell cytotoxicity during the effector phase and tumor elimination.

INTRODUCTION

CD8$^+$ T cells are powerful components of the adaptive immune system that have the potential to selectively eradicate cancer cells. However, despite the presence of tumor-specific CD8$^+$ T cells in tumor-bearing hosts, cancers develop, suggesting that CD8$^+$ T cells become dysfunctional and unresponsive to cancer cells over the course of tumorigenesis.[1] Tumor-infiltrating dysfunctional CD8$^+$ T cells commonly express high levels of inhibitory receptors (PD-1, LAG3, CTLA-4, and TIM3) and fail to produce effector cytokines (interferon-γ [IFNγ] and tumor necrosis factor-α [TNFα]) and cytotoxic molecules (granzymes and perforin). These hallmarks of CD8$^+$ T cell dysfunction have been attributed to chronic tumor antigen encounter/ T cell receptor (TCR) signaling and immunosuppressive signals within the tumor microenvironment.[1–3]

Adoptive T cell transfer (ACT), the infusion of large numbers (>10^9–10^{10} CD8$^+$ T cells/patient) of tumor-reactive cytolytic effector CD8$^+$ T cells into cancer patients, has emerged as a powerful therapeutic strategy for the treatment of cancers.[4] Tumor-reactive CD8$^+$ T cells can either be isolated from patients' own tumors (tumor-infiltrating lymphocytes [TILs]) or blood, expanded *ex vivo* and infused back, or engineered *in vitro* to become tumor-reactive through the introduction of genes encoding TCR or chimeric antigen receptors (CARs) specific for tumor antigens.[5–11] Although remarkable successes with ACT have been observed in a subset of cancer patients and cancer types (e.g., leukemia, lymphoma, and melanoma),[12–14] most patients still fail to achieve long-term responses, especially those with (non-melanoma) solid tumors. Factors that mitigate the efficacy of adoptively transferred CD8$^+$ T cells include poor *in vivo* persistence, poor

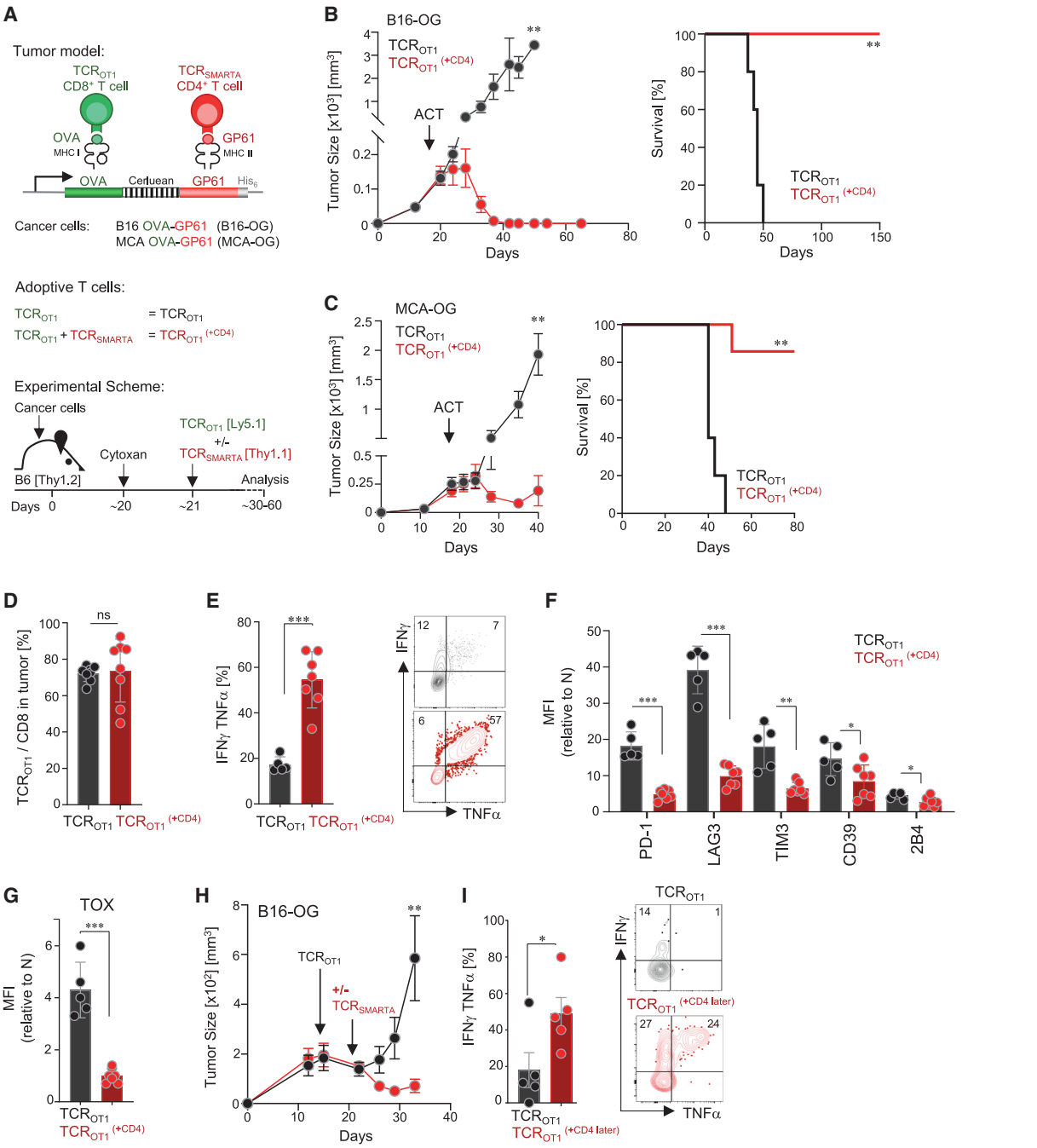

Figure 1. Tumor-specific CD4$^+$ T cells prevent and reverse CD8$^+$ T cell dysfunction within solid tumors and mediate tumor elimination

(A) Scheme: tumor models, adoptively transferred effector T cells, and experimental schemes.

(B) B16 OVA-GP$_{61-80}$ (B16-OG) tumor growth (right) and Kaplan-Meier survival curve (left) of tumor-bearing B6 WT mice (CD45.2; Thy1.2) receiving effector TCR$_{OTI}$ CD8$^+$ T cells alone (CD45.1) (black; TCR$_{OT1}$) or together with TCR$_{SMARTA}$ CD4$^+$ T cells (Thy1.1) (red; TCR$_{OT1}$$^{(+CD4)}$) (ACT = adoptive T cell transfer). Data are representative of 5 independent experiments (n = 5 mice/group). Data are represented as mean ± SEM. Significance is calculated by two-way ANOVA with Bonferroni correction (**$p \leq 0.0001$). Kaplan-Meier curve; **$p = 0.00021$; Mantel-Cox test.

(C) MCA205 OVA-GP$_{61-80}$ (MCA-OG) tumor outgrowth (significance is calculated by two-way ANOVA with Bonferroni correction (**$p \leq 0.0001$), and survival in B6 mice treated as described in (B); **$p = 0.0003$; Mantel-Cox test. Data are representative of 2 independent experiments (n = 5–6 mice/group).

(D) TCR$_{OT1}$ (% of total of CD8$^+$ T cells) within progressing B16-OG tumors 8–9 days post transfer +/− TCR$_{SMARTA}$ CD4$^+$ T cells. Data pooled from 2 independent experiments (n = 8 mice/group). Each symbol represents an individual mouse.

(E) IFNγ and TNFα production of TCR$_{OT1}$ isolated from B16-OG tumors 8–9 days post transfer +/− TCR$_{SMARTA}$ CD4$^+$ T cells. Cytokine production was assessed after 4-h peptide stimulation *ex vivo*. Gates are set based on negative controls (no stimulation or non-antigen-specific T cell population controls). Data show 2 pooled independent experiments (n = 5–7); representative flow plots are shown.

(legend continued on next page)

tumor localization or infiltration, and rapid loss of effector function.[13,15,16] Various therapeutic strategies have been identified to improve tumor infiltration and persistence, such as lymphodepletion and/or administration of homeostatic cytokines (IL-2, IL-7, and IL-15).[12,15,17–21] However, the loss of effector function of $CD8^+$ T cells remains a major roadblock.[22,23] Thus, the development of immunotherapeutic interventions to prevent or reverse $CD8^+$ T cell dysfunction has become the concerted effort of many clinicians and scientists.

While direct cytotoxic activity against cancer cells generally resides within the $CD8^+$ T cell compartment, various modes of action have been described for $CD4^+$ T cells[24]: (1) productive priming and activation of naive $CD8^+$ T cells in lymphoid tissues through "licensing" and functional maturation of dendritic cells (DCs),[25–32] (2) anti-tumor effector functions and elimination of MHC class II-negative cancer cells without $CD8^+$ T cells[33–37] through IFNγ acting on the host stroma, or activation of macrophages and other non-lymphoid tumoricidal effector cells,[36,38–43] and (3) induction of cancer cell senescence rather than cancer cell elimination through the secretion of Th1-cytokines (TNFα and IFNγ).[44,45] Moreover, we and others have demonstrated that $CD4^+$ T cells might play an important role during $CD8^+$ T cell-mediated tumor elimination as well as during autoimmune tissue destruction, however, the mechanisms remain elusive.[46–48] MHC class II-restricted tumor antigens and tumor-specific $CD4^+$ T cells have been identified in many cancer patients and cancer types, and their importance in anti-tumor immunity has been recognized.[24,33,49–53] If and how tumor-reactive $CD4^+$ T cells can be utilized to prevent or reverse $CD8^+$ T cell dysfunction leading to tumor eradication is less clear. To address this question, we developed a clinically relevant ACT-cancer mouse model. We demonstrate that $CD4^+$ T cells mediate tumor-specific $CD8^+$ T cell reprogramming within large solid tumors when tumor-reactive $CD4^+$ and $CD8^+$ T cells form three-cell-type clusters (triads) together with antigen-presenting cells (APCs). Triad formation resulted in the molecular and functional reprogramming of adoptively transferred $CD8^+$ T cells, preventing and even reversing T cell dysfunction, leading to tumor destruction. Importantly, triad formation was also critical for immune checkpoint blockade (ICB)-mediated anti-tumor immunity: established tumors were eliminated following anti-PD-1/anti-PD-L1 monoclonal antibody (mAb) treatment only when intratumoral $CD4^+$ T cell::$CD8^+$ T cell::APC triads could form. Strikingly, the formation of $CD4^+$ T cell::$CD8^+$ T cell::APC triads in tumors of patients with pleural mesothelioma treated with ICB was associated with clinical responses, uncovering $CD4^+$ T cell::$CD8^+$ T cell::APC triads as a key determinant for cancer elimination and ACT and ICB efficacy against solid tumors.

RESULTS

Tumor-specific $CD4^+$ T cells prevent and reverse tumor-specific $CD8^+$ T cell dysfunction in solid tumors

B16F10 (hereon "B16") is a highly aggressive murine melanoma cell line; B16 cancer cells injected subcutaneously into immunocompetent C57BL/6 wild-type mice (B6 WT) form large established tumors within 2 weeks, ultimately killing the host, and treatment regimens are generally ineffective. We engineered B16 cancer cells to express the $CD8^+$ T cell-recognized epitope from ovalbumin $OVA_{257-264}$ (SIINFEKL) as well as the $CD4^+$ T cell-recognized glycoprotein epitope $GP_{61–80}$ (GLKGPDIYKGVYQFKSVEFD) from the lymphocytic choriomeningitis virus (LCMV). The vector was constructed to encode the trimeric peptide sequence $(SIINFEKL\text{-}AAY)_3$ fused to the fluorescent protein Cerulean, followed by the 20-mer $GP_{61–80}$ peptide (Figure 1A). The $OVA_{257-264}$ epitope is presented on the MHC class I molecule H-$2K^b$ and recognized by TCR transgenic OT1 $CD8^+$ T cells (TCR_{OT1}); the $GP_{61–80}$ epitope is presented on the MHC class II molecule I-A^b and recognized by TCR transgenic SMARTA $CD4^+$ T cells (TCR_{SMARTA}). B16-$OVA_{257-264}$-$GP_{61–80}$ cancer cells (B16-OG; 2.5×10^6 cells/host) were injected subcutaneously into B6 WT (CD45.2) mice. Despite the expression of strong $CD8^+$- and $CD4^+$-T cell tumor antigens, B16-OG tumors grew aggressively, forming large tumors within 2 weeks (Figure 1B). We then employed an ACT regimen modeled on that used in cancer patients treated with ACT. We induced lymphopenia through a nonmyeloablative dose of cyclophosphamide (for better engraftment and efficacy of donor T cells[54]), followed by the infusion of *in vitro* generated cytotoxic tumor-specific $CD8^+$ T cells (Figure 1A). Naive congenic (CD45.1) TCR_{OT1} were activated *in vitro* for 3–4 days and adoptively transferred into lymphopenic B16-OG tumor-bearing mice. Despite the infusion of highly functional effector TCR_{OT1} $CD8^+$ T cells, B16-OG tumors progressed, recapitulating the scenario commonly observed in patients with solid tumors receiving ACT (Figure 1B). Next, we asked whether the simultaneous infusion of *in vitro* activated effector TCR_{SMARTA} $CD4^+$ T cells (Thy1.1) would mediate anti-tumor responses. Co-transfer of effector TCR_{OT1} together with TCR_{SMARTA} resulted in complete tumor elimination, with 100% long-term tumor-free survival (Figure 1B). Tumor-bearing mice that received TCR_{SMARTA} alone (Figure S1A) or TCR_{OT1} together with transgenic TCR_{OT2} $CD4^+$ T cells which recognize an irrelevant MHC-II I-A^b-restricted antigen (ovalbumin 323-339 peptide) (Figure S1B) did not show tumor regression, demonstrating that cancer elimination was dependent on both $CD8^+$ and $CD4^+$ antigen-specific T cells. We confirmed our results in a second tumor model using the fibrosarcoma cell line MCA205 (MCA205-OG) and obtained similar results (Figure 1C).

(F and G) Inhibitory receptor expression, and (G) TOX expression of B16-OG tumor-infiltrating TCR_{OT1} isolated 8–9 days post transfer +/− TCR_{SMARTA}. Graphs depict relative MFI normalized to naive TCR_{OT1} (N); two pooled independent experiments (n = 5–7 mice/group). (D–G) Values are mean ± SD. $^{***}p < 0.0001$; $^{**}p < 0.001$; $^{*}p < 0.05$.

(H) Mice with B16-OG tumors received effector TCR_{OTI} $CD8^+$ T cells 14 days post tumor transplantation; 8 days later, TCR_{SMARTA} $CD4^+$ T cells were adoptively transferred (red); B16-OG tumor growth in mice receiving only TCR_{OT1} are shown in black. Data are representative of 2 independent experiments (n = 8 mice/group). Values are mean ± SEM. Significance is calculated by two-way ANOVA with Bonferroni correction ($^{**}p \leq 0.0001$).

(I) IFNγ and TNFα production of TCR_{OT1} isolated from B16-OG tumors which did receive TCR_{SMARTA} $CD4^+$ T cells 6 days later (red); TCR_{OT1} which did not receive TCR_{SMARTA} $CD4^+$ T cells are shown in black. Data are representative of 2 experiments. Values are mean ± SEM; $^{*}p = 0.04$.

See also Figure S1.

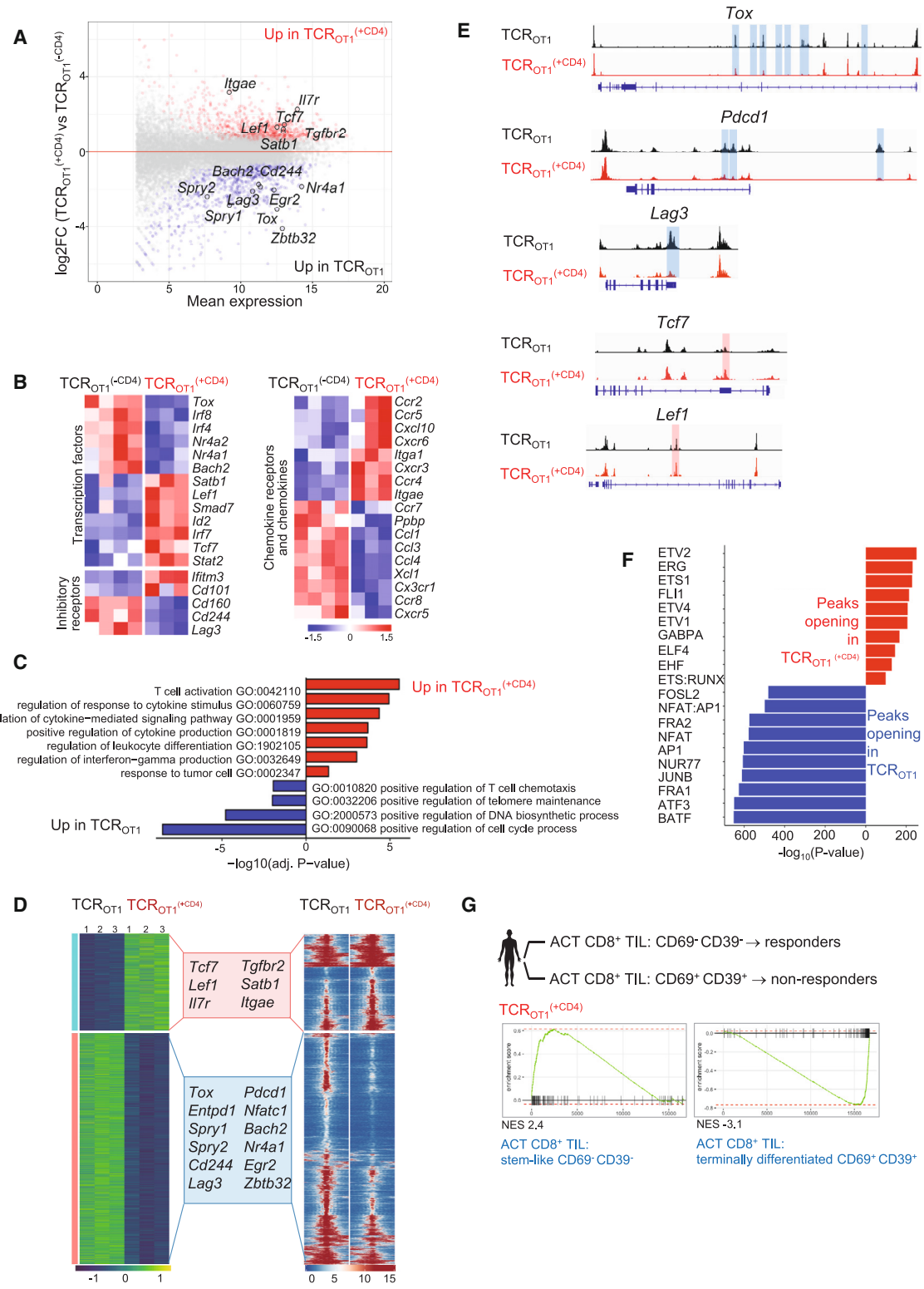

Figure 2. Tumor-specific CD4$^+$ T cells transcriptionally and epigenetically reprogram tumor-specific CD8$^+$ T cells and prevent terminal differentiation

(A) MA plot (scatterplot of log2 fold changes (M, on the y axis) versus the average expression signal (A, on the x axis)) of RNA-seq data showing the relationship between average expression and expression changes of TCR$_{OT1}$ and TCR$_{OT1}^{(+CD4)}$ TIL. Statistically significantly DEG (false discovery rate (FDR) < 0.05) is shown in red and blue, with select genes highlighted for reference.

(legend continued on next page)

CD4$^+$ T cells are known to enhance CD8$^+$ T cell mobilization into peripheral tissues.[31] To understand whether TCR_{SMARTA} enhanced TCR_{OT1} tumor infiltration, we compared the numbers of TCR_{OT1} TIL in mice which received effector TCR_{OT1} alone (TCR_{OT1}) or together with TCR_{SMARTA} ($TCR_{OT1}^{(+CD4)}$) by evaluating numbers of TIL 8–9 days post transfer, a time point when tumors are similar in size. Surprisingly, we found equal numbers of TCR_{OT1} TIL in both cohorts (Figure 1D), suggesting that TCR_{SMARTA}-mediated anti-tumor immunity was not due to an enhancement of TCR_{OT1} tumor infiltration but likely due to functional changes of TCR_{OT1} TIL. Indeed, while TCR_{OT1} TILs were impaired in their ability to produce the effector cytokines IFNγ and TNFα (Figure 1E), and expressed high levels of numerous canonical inhibitory receptors including PD-1, LAG3, TIM3, CD39, and 2B4 (Figure 1F), as well as the transcription factor TOX (Figure 1G), a critical regulator associated with T cell dysfunction and exhaustion,[55–60] $TCR_{OT1}^{(+CD4)}$ were able to produce high amounts of IFNγ and TNFα and showed little or no expression of inhibitory receptors and TOX (Figures 1E–1G). To understand whether these phenotypic and functional differences were already induced in the tumor-draining lymph node (tdLN), we compared phenotype and function of tdLN-TCR_{OT1} and tdLN-$TCR_{OT1}^{(+CD4)}$. No differences were observed in tdLN (Figure S1C). Thus, CD4$^+$ T cells specifically acted on tumor-specific CD8$^+$ T cells within the tumor.

Next, we wanted to understand whether CD4$^+$ T cells could not only prevent but also reverse CD8$^+$ T cell dysfunction/exhaustion. We adoptively transferred effector TCR_{OT1} into B16-OG tumor-bearing mice, and 6-8 days later, when TCR_{OT1} TILs were dysfunctional, we adoptively transferred effector TCR_{SMARTA}. Remarkably, mice that received TCR_{SMARTA} showed increased production of IFNγ and TNFα and tumor regression (Figures 1H and 1I). Thus, tumor-reactive TCR_{SMARTA} CD4$^+$ T cells can reverse tumor-induced CD8$^+$ T cell dysfunction and/or enhance recruitment of functional TCR_{OT1} from the periphery, ultimately leading to tumor regression.

CD4$^+$ T cells transcriptionally and epigenetically reprogram tumor-specific CD8$^+$ T cells, resulting in tumor elimination

Tumor-specific CD8$^+$ T cell dysfunction in mice and humans is associated with global transcriptional and epigenetic dysregulation of genes and pathways important for T cell differentiation and function. To understand how CD4$^+$ T cells mediated functional rescue of TCR_{OT1} CD8$^+$ T cells, we conducted RNA-seq and ATAC-seq of $TCR_{OT1}^{(+CD4)}$ and TCR_{OT1} TIL isolated from size-matched B16-OG tumors 7–8 days post transfer. 1,795 genes were differentially expressed (DEG) including exhaustion/dysfunction-associated transcription factors (TFs) and inhibitory receptors/activation markers (*Tox*, *Irf4*, *Lag3*, *CD160*, and *Cd244*) (Figures 2A and 2B), which were highly expressed in TCR_{OT1}. In contrast, TFs and molecules associated with stem-like progenitor T cell states were enriched and highly expressed in $TCR_{OT1}^{(+CD4)}$ TIL, including genes encoding *Tcf7* (TCF1), *Il7r*, *Itgae* (CD103), *Itga1*, and *Ifitm3*, as well as chemokine receptors such as *Ccr5*, *Ccr4*, and *Ccr2*.[28,61] Gene ontology (GO) classification revealed that pathways associated with positive cytokine regulation, immune differentiation, and responses to tumor cells were enriched in $TCR_{OT1}^{(+CD4)}$ but not in TCR_{OT1} (Figure 2C). ATAC-seq revealed 11,787 differentially accessible regions (DARs), including enhancers in many exhaustion (*Tox*, *Spry1*, *Spry2*, *Cd244*, *Bach2*, and *Egr2*) or stem-/progenitor cell state-associated genes (*Tcf7*, *IL7r*, and *Lef1*), respectively (Figures 2D and 2E). Many enhancer peaks with TF motifs associated with terminal differentiation were less accessible in $TCR_{OT1}^{(+CD4)}$, which was surprising given that $TCR_{OT1}^{(+CD4)}$ and TCR_{OT1} TIL were isolated from equally sized tumors (Figure 2F). To understand whether reprogrammed $TCR_{OT1}^{(+CD4)}$ revealed molecular signatures similar to human CD8$^+$ TIL driving clinical responses in the context of ACT, we utilized a dataset from a study conducted by the Rosenberg group, using *ex vivo*-expanded autologous CD8$^+$ TIL from metastatic melanoma lesions for ACT into preconditioned, lymphodepleted patients.[62] The authors identified a CD39$^-$ CD69$^-$ stem-like TIL subset that was associated with complete cancer regression in ACT-responders but lacking in ACT-non-responders. Gene set enrichment analysis (GSEA) revealed that similar genes were enriched in $TCR_{OT1}^{(+CD4)}$ CD8$^+$ TIL as in ACT (CD39$^-$ CD69$^-$) CD8$^+$ TIL responders, and genes in CD8$^+$ TIL from ACT (CD39$^+$ CD69$^+$) non-responders were enriched in TCR_{OT1} CD8$^+$ TIL (Figures 2G and S2).[62] Taken together, tumor-specific TCR_{SMARTA} CD4$^+$ T cells transcriptionally and epigenetically reprogram tumor-reactive CD8$^+$ TIL within progressing tumors, preventing terminal differentiation, resulting in tumor elimination.

Spatial positioning of tumor-specific CD8$^+$ and CD4$^+$ T cells within tumors determines anti-tumor immunity and cancer elimination

Next, we wanted to understand *how* TCR_{SMARTA} CD4$^+$ T cells prevent CD8$^+$ T cell dysfunction within tumors. B16 tumor cells express low level MHC II *in vivo* (Figure S3A), thus cancer cells could become targets of CD4$^+$ T cells. Employing CRISPR-Cas9-mediated gene editing, we generated MHC class

(B) Heatmap of RNA-seq expression (normalized counts after variance stabilizing transformation, centered and scaled by row for DEG) (FDR <0.05) in TCR_{OT1} and $TCR_{OT1}^{(+CD4)}$ TIL.
(C) Selected GO terms enriched for genes upregulated in TCR_{OT1} (blue) and $TCR_{OT1}^{(+CD4)}$ (red) TIL.
(D) Chromatin accessibility (ATAC-seq); (left) heatmap of log2-transformed normalized read counts transformed with variance stabilization per for regions with differential chromatin accessibility; (right) each row represents one peak (differentially accessible between TCR_{OT1} and $TCR_{OT1}^{(+CD4)}$ TIL; FDR <0.05) displayed over a 2-kb window centered on the peak summit; regions were clustered with k-means clustering. Genes associated with the two major clusters are highlighted.
(E) ATAC-seq signal profiles across the *Tox*, *Pdcd1*, *Lag3*, *Tcf7*, and *Lef1* loci. Peaks significantly lost or gained are highlighted in red or blue, respectively.
(F) Top 10 most-significantly enriched transcription factor motifs in peaks with increased accessibility in $TCR_{OT1}^{(+CD4)}$ TIL (red) or TCR_{OT1} TIL (blue).
(G) Enrichment of gene sets in $TCR_{OT1}^{(+CD4)}$, described for human tumor infiltrating CD8$^+$ TIL; (CD69$^-$ CD39$^-$) stem-like TIL (responders) or (CD69$^+$ CD39$^+$) terminally differentiated TIL (non-responders) from metastatic melanoma patients receiving *ex vivo* expanded TIL for ACT.[62] NES, normalized enrichment score. See also Figure S2.

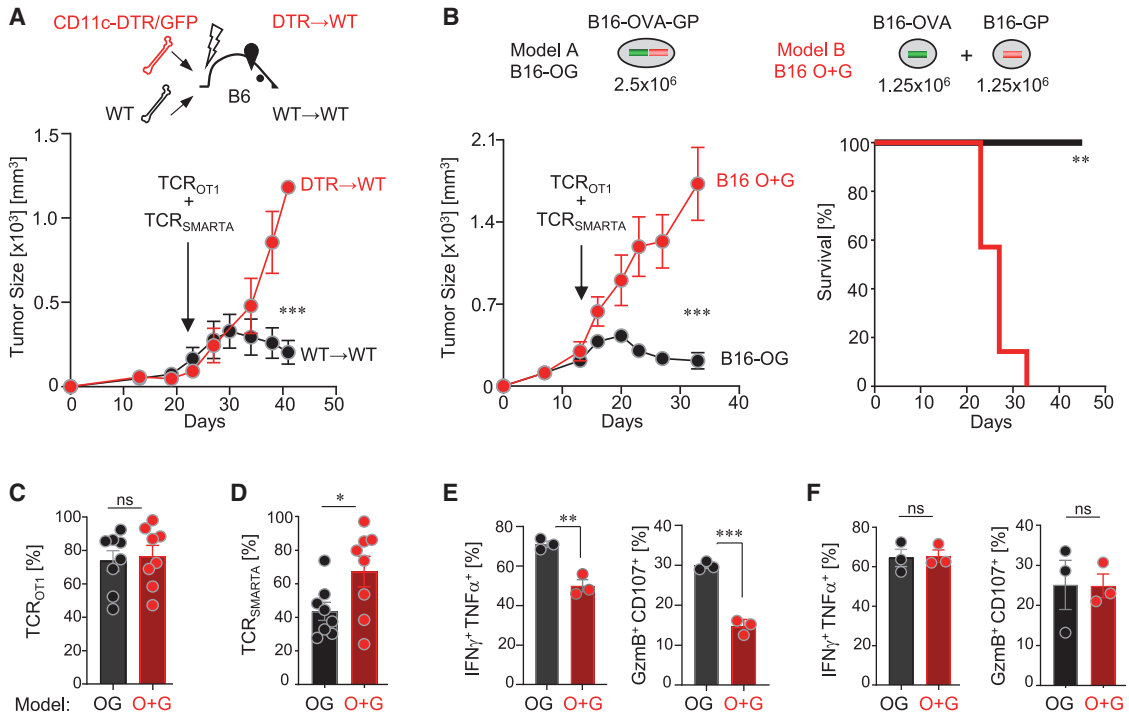

Figure 3. Tumor elimination requires unique spatial orientation of tumor-specific CD8⁺ T cells, tumor-specific CD4⁺ T cells, and CD11c⁺ dendritic cells (DC) within tumors

(A) B16-OG tumor outgrowth in CD11c-DTR/GFP bone marrow (BM) chimeras (scheme, top; DTR→WT or WT→WT) treated with diphtheria toxin (DT). *In vitro* activated TCR_{OTI} and TCR_{SMARTA} were adoptively transferred into lymphodepleted tumor-bearing BM chimeras. 5 days post ACT, mice were treated with DT. Representative of 2 independent experiments (n = 3 mice/group). Values are mean ± SEM. Significance is calculated by two-way ANOVA with Bonferroni correction ($p \leq 0.0001$).

(B) (Top) Experimental scheme of tumor models A and B: 2.5 × 10^6 B16-OG cancer cells (B16-OG; model A) or 1.25 × 10^6 B16-OVA (B16-O) mixed with 1.25 × 10^6 B16-GP_{61-80} cancer cells (B16 O+G; model B) were transplanted into B6 WT mice. (Bottom), Tumor outgrowth of B16-OG or B16 O+G tumors after TCR_{OTI} and TCR_{SMARTA} ACT. Kaplan-Meier survival curve. Representative of 2 independent experiments (n = 7 mice/cohort). Data are shown as mean ± SEM. Significance is calculated by two-way ANOVA with Bonferroni correction ($p \leq 0.0001$). (Right) Kaplan-Meier curve; **p = 0.0002; Mantel-Cox test.

(C) Percentage of $TCR_{OT1}^{(+CD4)}$ (out of total CD8⁺ TIL) 9 days post ACT.

(D) Percentage of TCR_{SMARTA} (out of total CD4⁺ TIL) 9 days post ACT. Data represent 2 pooled, independent experiments (n = 8 mice/tumor model). Each symbol represents an individual mouse.

(E and F) IFNγ, TNFα, CD107, granzyme B production of $TCR_{OT1}^{(+CD4)}$ isolated from B16-OG or B16 O+G tumors, or (F) isolated from tumor-draining lymph nodes of B16-OG or B16 O+G tumor-bearing hosts. Cytotoxic molecules and cytokine production assessed after 4-h peptide stimulation *ex vivo*. Representative of 2 independent experiments (n = 3 mice/tumor). Data are shown as mean ± SEM. ***$p < 0.0005$, **$p < 0.005$, *$p < 0.05$, unpaired two-tailed Student's t test. ns, not significant.

See also Figures S3 and S4.

II *I-A*^{b}-deficient B16-OG cancer cells (Figure S3B). Surprisingly, large established B16-OG *I-A*^{b}-deficient tumors were eliminated as efficiently as parental MHC class II-expressing B16-OG tumors, demonstrating that cancer elimination does not require CD4⁺ T cells to directly target cancer cells (Figure S3C). Next, we turned to the tumor stroma, which includes MHC class I- and II-expressing APC such as CD11c⁺ DC and macrophages. To assess the role of CD11c⁺ cells, we employed a targeted depletion approach: CD11c⁺ DC from CD11c-DTR/GFP transgenic mice express the primate diphtheria toxin receptor (DTR) transgene under the CD11c promoter, enabling conditional depletion of CD11c⁺ cells *in vivo* upon DT treatment.[63] We generated bone marrow (BM) chimeras by transferring BM cells from CD11c-DTR/GFP (CD11c-DTR) or littermate control (WT) mice into lethally irradiated WT (CD45.1) B6 mice (designated "DTR→WT" and "WT→WT" chimeras). B16-OG tumors were established in DTR→WT and WT→WT BM chimeras, and 2–3 weeks post B16-OG tumor cell transplantation effector TCR_{OT1} and TCR_{SMARTA} were adoptively transferred. 5 days post ACT, when TCR_{OT1} and TCR_{SMARTA} infiltrated into tumors, mice were treated twice weekly with DT. Depletion of CD11c⁺ APC prevented tumor elimination in DTR→WT mice but not control WT→WT mice, suggesting that CD11c⁺ APC within the tumor microenvironment were necessary for TCR_{SMARTA}-mediated TCR_{OT1} reprogramming and tumor elimination (Figure 3A).

Next, we wanted to investigate how TCR_{SMARTA}, $TCR_{OT1}^{(+CD4)}$, and stromal cell interactions cause tumor elimination. To answer this question, we modified our tumor model (Figure 3B): we generated B16 tumor cell lines expressing either the CD8 epitope OVA (B16-O) or CD4 epitope GP (B16-G) tumor antigens (fused to EGFP or Cerulean, respectively). We implanted a

mixture of 1.25 × 10^6 B16-O and 1.25 × 10^6 B16-G cancer cells into WT B6 mice, forming mixed B16 O+G tumors. Control mice received 2.5 × 10^6 B16-OG tumor cells as in Figures 1 and 2. We confirmed that B16 O+G and B16-OG tumors expressed overall similar amounts of OVA- and GP-antigens by comparing activation and proliferation of naive CTV-labeled TCR_{OT1} and TCR_{SMARTA} *in vivo* (Figures S3D and S3E). Thus, both cohorts received the same total number of cancer cells (2.5 × 10^6), expressing similar levels of OVA and GP tumor antigens. B16 O+G tumors grew with similar kinetics as B16-OG tumors. 2–3 weeks post tumor transplantation, mice received effector TCR_{OT1} and TCR_{SMARTA}. Equal numbers of TCR_{OT1} and TCR_{SMARTA} TIL were found within progressing B16 O+G and B16-OG tumors 9 days post-ACT (Figures 3C and 3D). Strikingly, despite the same numbers of tumor cells, equal tumor antigen levels and tumor sizes, and same numbers of TCR_{OT1} and TCR_{SMARTA} TIL, mixed B16 O+G tumors continued to grow, in contrast to B16-OG tumors, which ultimately regressed (Figure 3B). TCR_{OT1} TIL isolated from B16 O+G tumors revealed a dysfunctional phenotype similar to those described for TCR_{OT1} transferred without $CD4^+$ T cells shown in Figure 1 (Figure 3E). Importantly, these functional differences were only observed within the tumor and not in the tdLN (Figure 3F). We conducted phenotypic characterization of intratumoral DC (CD86, CD70, and CD40) and TCR_{SMARTA} $CD4^+$ T cells (CD27, TBET, and PD-1) of B16-OG and B16 O+G tumors and did not find significant differences in the expression of these molecules (Figures S4A–S4C).

What are the factors and mechanisms that determine tumor progression or regression if numbers of cancer cells and antigen-specific $CD8^+$ and $CD4^+$ TIL are similar? We hypothesized that a unique spatial organization of cancer cells, $CD4^+$ T cells, $CD8^+$ T cells, and DC within tumors likely drove $CD8^+$ T cell reprogramming and tumor destruction.

Intratumoral immune triads are required for $CD8^+$ T cell cytotoxicity and tumor elimination

To define the intratumoral spatial characteristics we conducted confocal microscopic analysis of established B16 O+G tumors. We found regions of either B16-OVA-positive or B16-GP-positive cancer cells and very few regions that had B16-OVA and B16-GP cancer cells intermingled (Figure S4D). Progressing B16 O+G tumors retained the initial B16-OVA:B16-GP (1:1) cancer cells ratio, suggesting that TCR_{OT1} and TCR_{SMARTA} were unable to eliminate B16-OVA or B16-GP cancer cells, respectively (Figure S4E). The mosaic-like appearance of distinct tumor regions is a typical feature of clonally growing cancer cells in transplantation tumor models.[46] Consequently, in B16 O+G tumors CD8 or CD4 antigens are largely presented in distinct regions within the tumor and on distinct DC/APC (Model B), unlike in B16-OG tumors where CD8 and CD4 antigens are co-presented on the same DC/APC through epitope linkage (Model A) (Figure 4A). Thus, we propose the following model: co-presentation of tumor-specific CD4 and CD8 tumor antigens on the same APC will "force" antigen-specific $CD4^+$ and $CD8^+$ T cells to form three-cell-type clusters (triads) with APC, and the physical proximity of $CD8^+$ T cells with $CD4^+$ T cells drives $CD4^+$ T cell-mediated $CD8^+$ T cell reprogramming and cancer cell destruction (Model A). In Model B, $CD8^+$ and $CD4^+$ T cells fail to form triads with APC, and $CD4^+$ T cells are unable to mediate $CD8^+$ T cell reprogramming, ultimately allowing tumors to progress. The concept of a "three-cell-type cluster" was first described in 1987: Mitchison and O'Malley suggested that three-cell-type clusters of $CD4^+$ T cell::$CD8^+$ T cells::APC were required for the cytolytic response of $CD8^+$ T cells in an allogeneic transplant setting.[64] However, little is known about their functional relevance *in vivo* and/or underlying mechanisms.

To determine whether triads are required for tumor elimination, we generated color-coded B16 O+G and B16 O-G tumor models: TCR_{SMARTA} transgenic mice were crossed to EGFP transgenic mice, generating EGFP-expressing TCR_{SMARTA} $CD4^+$ T cells; TCR_{OT1} were engineered to express the red fluorescent protein (RFP); CD11c-YFP mice were used as hosts (with yellow fluorescent protein (YFP) under the transcriptional control of the CD11c promoter, thereby YFP-labeling CD11c+ host cells). B16-OG, B16-O, and B16-G cancer cells expressed Cerulean. B16-OG or B16 O+G tumors were established in CD11c-YFP mice and effector TCR_{OT1}-RFP^+ and TCR_{SMARTA}-$EGFP^+$ were adoptively transferred (Figure 4B). Strikingly, 8–9 days post-ACT, significantly higher numbers of TCR_{OT1}::$CD11c^+YFP^+$::TCR_{SMARTA} triads (~30 interactions/field (or close apposition)) were present in B16-OG tumors, which eventually regressed, in contrast to B16 O+G tumors (~7 interactions), which eventually progressed (Figure 4C). When normalized to the total number of infiltrating $CD11c^+YFP^+$ cells/field, which remained constant in both tumor models (Figure 4D, right), we observed a 3.5-fold increase of triads in B16-OG tumors (Figure 4D, left). Importantly, dyads, two-cell interactions between TCR_{SMARTA}::$CD11c^+YFP^+$ DC, were not significantly different between B16-OG and B16 O+G (Figure 4E). Thus, $CD4^+$ T cell::$CD8^+$ T cell::DC triads are associated with tumor-specific $CD8^+$ T cell reprogramming and tumor elimination.

To further confirm that $CD4^+$ T cells are required during the $CD8^+$ T cell effector phase within tumors, we conducted contralateral transplantation experiments. We injected B16-OG cancer cells into one flank and B16-O cancer cells into the opposite flank of the same mouse; if $CD4^+$ T cells were required during the effector phase through intratumoral triad formation, only B16-OG but not B16-O tumors should be eliminated. Indeed, B16-O grew progressively post TCR_{OT1} and TCR_{SMARTA} ACT, while contralateral B16-OG tumors were rejected (Figure 4F). Moreover, when TCR_{SMARTA} were co-transferred with TCR_{OT1} into tumor-bearing B16-OG hosts and then depleted 5–6 days post-transfer through $CD4^+$-depleting monoclonal antibody treatment, tumors initially regressed but eventually progressed, suggesting that continuous/sustained intratumoral triad formation and $CD4^+$ T cells are required for $CD8^+$ T cell-mediated tumor destruction (Figure S4F).

Immune checkpoint blockade (ICB) therapies (e.g., anti-PD-1/anti-PD-L1/anti-CTLA-4 mono- or combination therapies) can empower endogenous tumor-specific $CD8^+$ T cells and $CD4^+$ T cells to effectively recognize and attack tumors.[65] ICB therapies have shown efficacy in some cancer patients and cancer types, however, most patients remain refractory.[66–68] The underlying mechanisms determining ICB resistance or responsiveness, as well as predictive biomarkers, remain poorly defined.

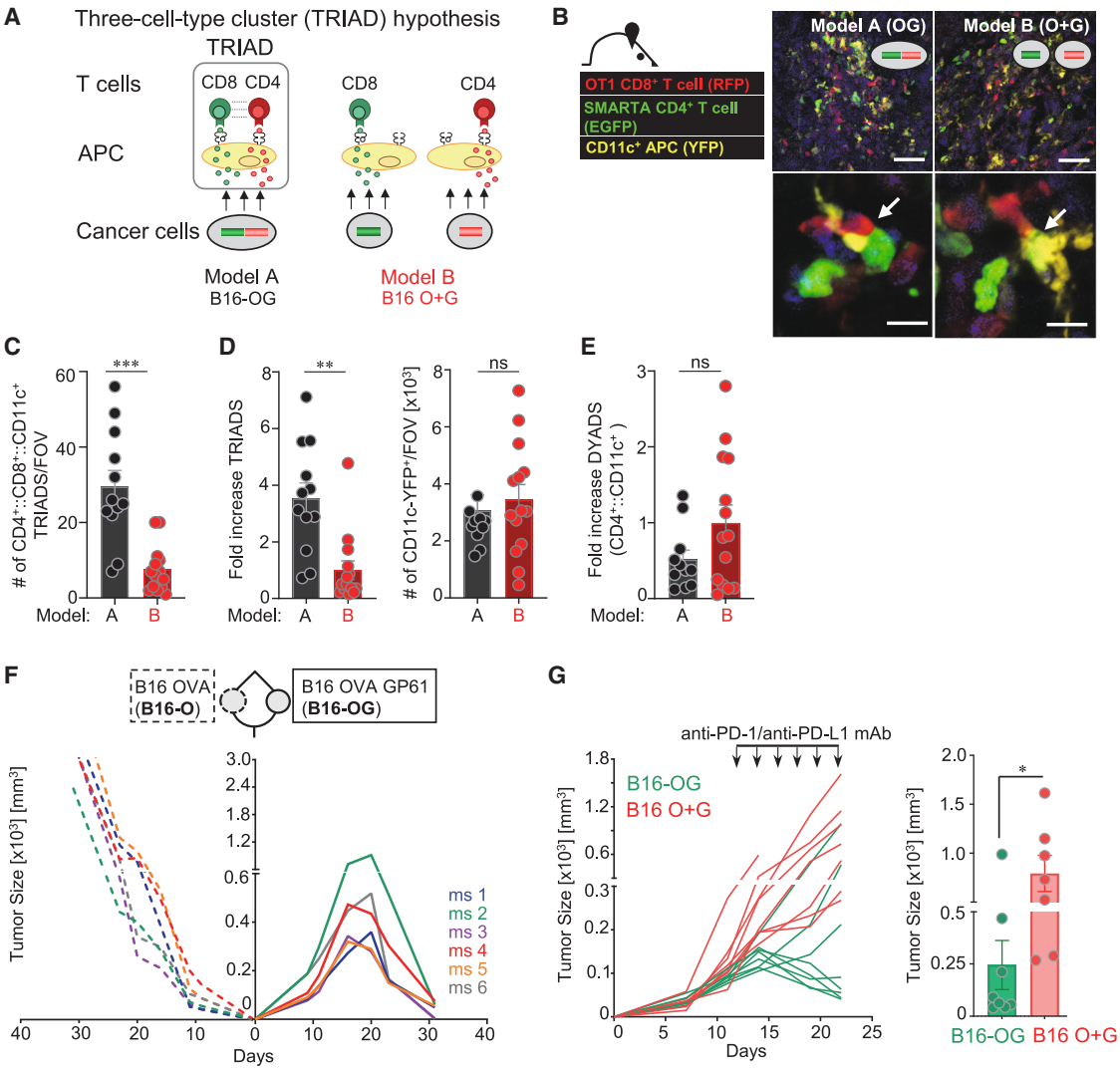

Figure 4. Intratumoral immune triads (three-cell-type clusters; CD4⁺ T cell::CD8⁺ T cell::DC) are required for CD8⁺ T cell reprogramming, cytotoxicity, and tumor elimination

(A) Proposed model: Triad formation (three-cell-type clusters; CD4⁺ T cells::CD8⁺ T cells::DC) form in B16-OG tumors (model A) where CD8 and CD4 tumor antigens/epitopes are linked and co-presented on the same APC within tumors; tumor-specific CD8⁺ and CD4⁺ T cells engage on same DC/APC; CD4⁺ T cells reprogram CD8⁺ T cells. Model B: B16 O+G; triads cannot form because CD8 and CD4 tumor antigens are presented on distinct APC.

(B) Color-coded mouse models to determine intratumoral immune triad formation (models A and B). B16-OG (model A) or B16 O+G (model B) tumors were established in CD11c-YFP mice (yellow); effector TCR_{OT1}-RFP (red) and TCR_{SMARTA}-EGFP T cells (green) were adoptively transferred into tumor-bearing hosts. Confocal microscopy analysis of frozen tumor tissue sections (tumors were analyzed 8–9 days post T cell transfer). Arrows indicate cell-cell interactions within B16-OG tumors. Scale bars indicate 50 μm (top); 10 μm (bottom).

(C and D) Numbers of triads per field of view (FOV), and (D) (left) Fold increase of triads normalized to total numbers of CD11c-YFP⁺ cells/FOV (right).

(E) Quantification of fold increase of numbers of CD4⁺ T cell-DC dyads normalized to total number of infiltrating CD11c-YFP⁺ cells/FOV. Each symbol represents an individual frozen tumor section (n = 3 mice/group/model). Data are shown as mean ± SEM. ***p < 0.0001, **p < 0.001, unpaired two-tailed Student's t test.

(F) Growth of B16-OG tumors (solid lines; right) and contralateral B16-O tumors (dashed lines; left) in B6 WT mice (n = 6) receiving adoptively transferred *in vitro* activated TCR_{OT1} and TCR_{SMARTA} T cells 14 days post tumor transplantation. Data are representative of 3 independent experiments.

(G) Outgrowth of B16-OG (green) and B16 O+G (red) tumors in B6 WT mice receiving anti-PD-1 and anti-PD-L1 blocking monoclonal antibodies (mAb) at indicated time points (days 12, 14, 16, 18, 20, and 22 post tumor transplantation; black arrows). Data are representative of 2 independent experiments. (Right) Tumor volume at day 22 post tumor implantation following ICB. Data are shown as mean ± SEM. *p = 0.02, using unpaired two-tailed Student's t test.

See also Figure S4.

We asked whether triad formation was critical for ICB-mediated anti-tumor responses. Mice with established B16-OG or B16 O+G tumors were treated with anti-PD-1/anti-PD-L1 blocking monoclonal antibodies (mAb). Strikingly, B16-OG tumors (which can form triads) were rejected following ICB treatment, but not B16 O+G tumors (which cannot form triads) (Figure 4G), highlighting the importance of triads for ICB-mediated cancer elimination.

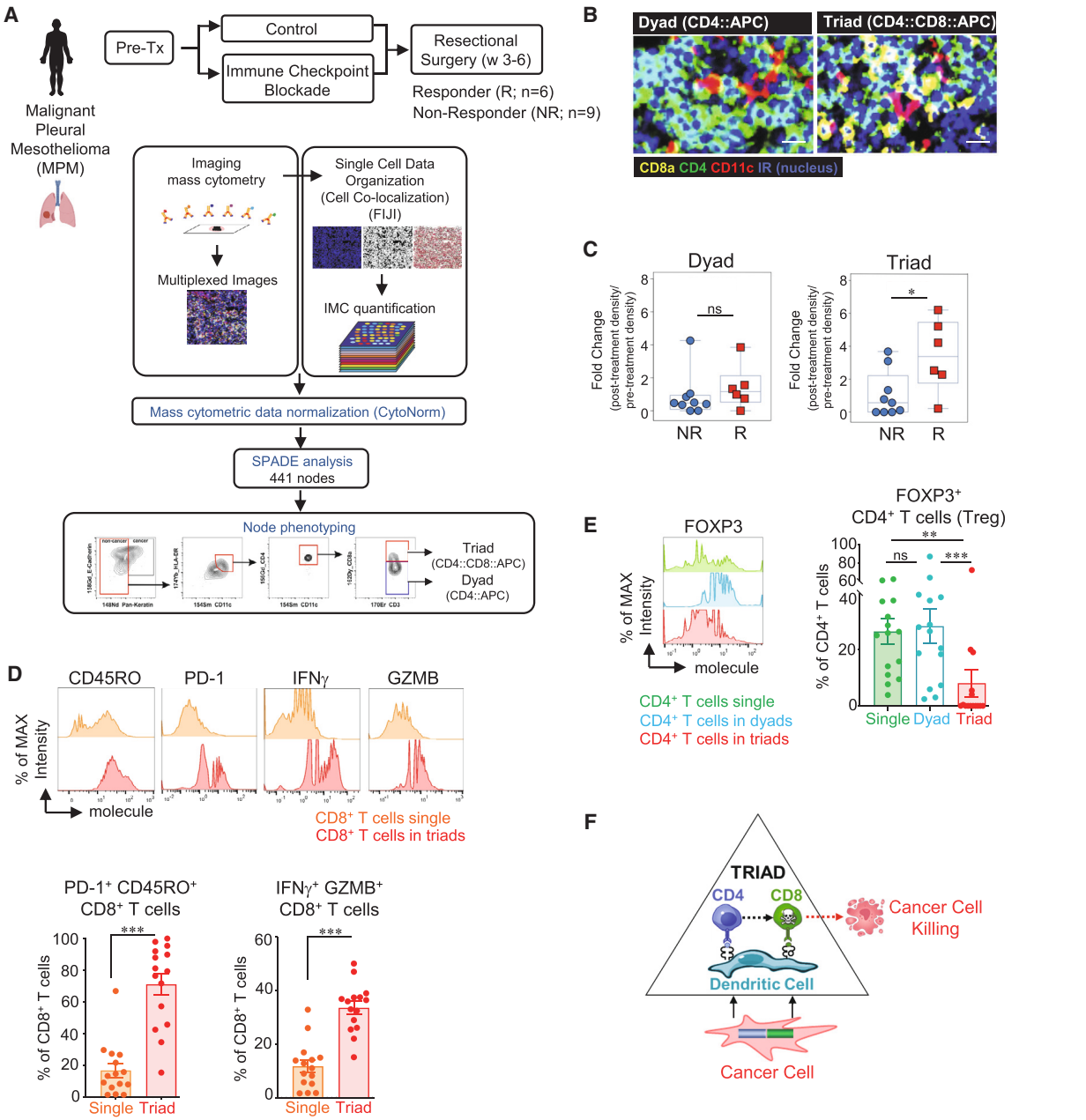

Figure 5. Intratumoral triads are associated with pathologic responses to immune checkpoint blockade in patients with malignant pleural mesothelioma (MPM)

(A) Treatment regimen and methodology used to determine triads (CD4⁺ T cell::CD8⁺ T cell::APC) and dyads (CD4⁺::APC). Pipeline of co-localization detection by multiplexed imaging mass cytometry (IMC; see STAR Methods for more details). Briefly, FFPE tumor tissues were stained with 35 target-specific antibodies. Automated cluster detection estimated cluster boundaries by expanding the perimeter of nuclei, identified by Cell ID Intercalator-iridium (191Ir). IMC images were quantified through FIJI, and protein expression data extracted through mean intensity multiparametric measurements performed on individual clusters. Acquired cluster data were normalized with CytoNorm tools, and normalized cytometric data transferred into additional Spanning-tree Progression Analysis of Density-normalized Events (SPADE) to generate automated clustering algorithm and applied cytometric analysis in FlowJo.

(B) Representative multiplexed mass cytometry images of triads and dyads. Scale bars indicate 50 μm.

(C) Fold change of triads and dyads of pre- and post-immune checkpoint therapy density (numbers/mm^2) in pathologic responders (R) and non-responders (NR). In box and whisker plots, the box spans from the lower quartile to the upper quartile, encompassing the interquartile range; a horizontal line within the box marks the median value. The whiskers extend from the box to the minimum and maximum values, showing the overall range. *p = 0.02; p = 0.34 (ns, not significant).

(D) Phenotypic analysis of intratumoral CD8⁺ T Cells using IMC. Expression of CD45RO, PD-1, IFNγ, and granzyme B (GZMB) on single CD8⁺ T cells within tumors (orange) or CD8⁺ T cells within triads (red). Data are shown as mean ± SEM; ****p < 0.0001, using paired two-tailed Student's t test.

(legend continued on next page)

Intratumoral triads in patients with pleural mesothelioma treated with ICB are associated with clinical responsiveness

Next, we asked whether CD4$^+$ T cell::CD8$^+$ T cell::APC triads could be associated with clinical responsiveness in humans. As clinical data assessing spatial characteristics of immune cells within tumors of ACT-treated patients were not available, we turned to patients treated with ICB therapy. We assessed the spatial orientation of CD8$^+$ T cells, CD4$^+$ T cells, and APC in patients with malignant pleural mesothelioma (MPM) undergoing ICB therapy.[69] Patients were randomized and treated with durvalumab (anti-PD-L1) mono- or durvalumab and tremelimumab (anti-CTLA-4) combination therapy. A no ICB group was included as a control cohort. Tumor tissues were obtained both before and after ICB treatment.[69] Evaluable tumors, before and after ICB were available for 15 patients receiving ICB. Out of the 15 patients, 6 patients showed a pathologic response (R; Responders) while 9 patients did not (NR; Non-Responders) (Figure 5A). Multiplexed imaging mass cytometry (IMC) was performed on all 15 patients' pre- and post-treatment tumor tissues using 35 markers to determine co-localization of non-T_{REG} CD4$^+$ T cells, CD8$^+$ T cells, and CD11c$^+$ APC, including the presence of dyads (CD4$^+$::APC) and triads (CD4$^+$::CD8$^+$::APC) (Figures 5A and 5B). Strikingly, while dyads were not associated with a pathologic response to ICB, triads were able to demarcate responders from non-responders (Figure 5C). We assessed the phenotypic characteristics of CD4$^+$ and CD8$^+$ T cells in single, dyad or triad compositions within tumors by IMC. We found that CD45RO$^+$ PD-1$^+$ CD8$^+$ T cells in triads expressed high(er) levels of IFNγ and granzyme B, compared to CD8$^+$ T cells in non-triad compositions (Figure 5D). Moreover, we observed a significantly lower presence of regulatory CD4$^+$ T cells (Treg) cells (based on FOXP3 expression) in triads compared to isolated single CD4$^+$ T cells or those within dyads (Figure 5E). Through cellular density analysis, we quantified the numbers of Treg cells within a radius of 100–400 μm centered on dyads or triads: dyads had a higher density of proximal Treg cells, whereas triads exhibited a reduced number of Treg cells in their vicinity (Figure S5). Our studies identify triads as critical determinants for anti-tumor immunity and ICB responsiveness in patients with MPM.

DISCUSSION

Our work uncovers intratumoral triads as a key requirement for anti-tumor immunity. We demonstrate that in addition to the known requirement of CD4$^+$ T cells for proper CD8$^+$ T cell priming and activation, CD4$^+$ T cells are also required during the effector phase to license CD8$^+$ T cell cytotoxicity and CD8$^+$ T cell-mediated cancer cell elimination. CD4$^+$ T cell-mediated reprogramming of CD8$^+$ T cells and cancer cell elimination is strictly dependent on the formation of immune triads where tumor-specific CD8$^+$ T cells and CD4$^+$ T cells must co-engage with the same DC. CD4$^+$ T cells do not have to engage with cancer cells, which is important, given that most epithelial cancers do not express MHC class II. We demonstrate that the spatial positioning of CD8$^+$ and CD4$^+$ T cells within tumors, and not their numbers, is the critical determinant for effective ACT- or ICB-mediated anti-tumor immunity. Our data may provide clues as to why ACT clinical trials utilizing predominantly tumor-reactive CD8$^+$ T cells have shown only limited responses for the treatment of solid tumors.

It is well established that CD4$^+$ T cells are required for CD8$^+$ T cell effector differentiation. However, studies have mainly focused on CD4$^+$ T cell "help" for CD8$^+$ T cells during the priming/activation phase and memory formation in infection and vaccination settings.[29,43,70–72] The importance of CD8$^+$ and CD4$^+$ T cell cooperation during the priming/activation phase was elegantly described by several groups. For example, the Berzofsky group demonstrated that for vaccines, CD8$^+$ and CD4$^+$ T cell-recognized peptides had to be physically linked to obtain optimal cytolytic CD8$^+$ T cell responses, as a mixture of CD8$^+$ and CD4$^+$ T cell peptides only elicited marginal CD8$^+$ T cell responses, suggesting co-engagement of CD8$^+$ and CD4$^+$ T cells on the same APC being critical during the priming/activation phase.[73] Moreover, the Germain group demonstrated that nonrandom, chemokine-driven (CCL3 and CCL4) recruitment of CCR5$^+$ naive, antigen-specific CD8$^+$ T cells to sites of antigen-specific DC-CD4$^+$ T cell interactions within antigen-draining lymph nodes led to optimal CD8$^+$ T cell responses during vaccination and early infections.[28] In line with these studies, vaccines relying only on short, single MHC class I-restricted peptides showed reduced clinical benefits compared to synthetic long peptide vaccine platforms containing both MHC class I and class II epitopes, further highlighting the importance of guided CD8$^+$ and CD4$^+$ cooperation.[74,75] CD4$^+$ T cells license DC through CD40L-CD40 interactions, enhancing B7 and CD70 expression on DC; CD28- and CD27-expressing antigen-specific CD8$^+$ T cells (ligands for B7 and CD70, respectively) receive optimal co-stimulatory signals when engaging with DC-CD4$^+$ T cells and/or abundant IL2 produced by CD4$^+$ T cells.[24] Here, we discover that CD4$^+$ T cells and triads are critical for cytolytic effector CD8$^+$ T cells and the physical proximity of CD8$^+$ T cells with CD4$^+$ T cells likely enforces chemokine and/or cytokine signaling, or direct receptor-ligand interactions needed for CD8$^+$ T cell reprogramming. Interestingly, chemokine receptors such as *Ccr5*, *Ccr4*, and *Ccr2* were upregulated on $TCR_{OT1}^{(+CD4)}$ encountering DC-CD4$^+$ T cells, as well as *Il2rg* and *Ifngr1*. Future studies will determine the precise mechanisms by which CD4$^+$ T cells and/or DC reprogram CD8$^+$ T cells, and how CD8$^+$ T cells resist T cell dysfunction and mediate cancer destruction.

Our mouse models utilized highly expressed CD8 and CD4 tumor model antigens and pure populations of TCR transgenic T cells for ACT to drive tumor elimination. However, human tumors are generally genetically and molecularly heterogeneous,

(E) Analysis of intratumoral CD4$^+$ T Cells. FOXP3 expression in single CD4$^+$ T cells (green), dyads (blue), and triads (red) compositions using IMC. CD4$^+$ T cells in triads exhibit lower expression of FOXP3. Data are shown as mean ± SEM. Two-way ANOVA, $p = 0.0141$, with Tukey's multiple comparisons tests as post hoc testing (single vs. dyad, ns ($p = 0.777$); single vs. triad, $^{**}p = 0.0013$; dyad vs. triad $^{****}p < 0.0001$).
(F) Proposed model of TRIAD-associated cancer elimination.
See also Figure S5.

and antigen quality and quantity can vary within progressing tumors. In addition, human tumors might not express CD8 and CD4 tumor antigens at high levels, raising the question whether intratumoral triads can sufficiently and effectively form in human tumors for ACT- or ICB-mediated tumor elimination. Our finding that triads (but not dyads) were associated with a pathogenic anti-tumor response in ICB-treated patients with pleural mesothelioma suggests that intratumoral immune triads indeed can form effectively to mediate anti-tumor responses. Interestingly, and congruent with our findings, another study demonstrated that dendritic cell–$CD4^+$ T helper cell niches enable $CD8^+$ T cell differentiation in patients with hepatocellular carcinoma following PD-1 blockade.[76]

Our study reveals a previously unappreciated role of unique cell-cell interactions and spatial positioning within tumors where tumor-specific $CD4^+$ T cells empower tumor-specific $CD8^+$ T cells to eliminate solid tumors. MHC class II-restricted tumor antigens and tumor-specific $CD4^+$ T cells have been described in human cancers.[49–51] Designing therapeutic interventions that enforce the formation of $CD4^+$ T cell::$CD8^+$ T cell::DC triads in tumors might be powerful strategies for the treatment of cancers, including for ICB, vaccine, and ACT approaches.

STAR★METHODS

Detailed methods are provided in the online version of this paper and include the following:

SUPPLEMENTAL INFORMATION

Supplemental information can be found online at https://doi.org/10.1016/j.ccell.2024.05.025.

ACKNOWLEDGMENTS

We thank the members of the Schietinger lab for helpful discussions; Remy Bosselut and Melanie Vacchio (Center for Cancer Research, National Cancer Institute, NIH) for providing reagents for revision experiments; M. Philip (Vanderbilt University) for critical reading of the manuscript. This work was supported by NIH grants DP2CA225212 and R01CA269733 (A.S.), Lloyd Old STAR Award of the Cancer Research Institute (A.S.), AACR-Bristol-Myers Squibb Midcareer Female Investigator Award (A.S.), Pershing Square Sohn Award (A.S.), Josie Robertson Young Investigator Award (A.S.), the Weill Cornell Medicine Core Laboratories Center (P.Z. and D.B.), Ludwig Cancer Center Postdoctoral Fellowship (G.E.C.); NIH Merit Award R37CA248478 (B.M.B.), Cancer Prevention and Research Institute of Texas Grant CPRIT RP200443 (H.S.L.), Department of Defense Peer Reviewed Cancer Impact Award CA210522 (H.S.L.), NIH R21AI159379 (H.S.L.), and the Helis Medical Research Foundation (H.S.L.). This project was also supported by the Cytometry and Cell Sorting Core at Baylor College of Medicine with funding from the NIH (NCI P30CA125123 and NCRR S10RR024574) and CPRIT (RP180672), and the assistance of Joel M. Sederstrom. We acknowledge the use of the MSKCC-Integrated Genomics Operation Core, funded by the NCI Cancer Center Support Grant (P30 CA08748), Cycle for Survival, and the Marie-Josée and Henry R. Kravis Center for Molecular Oncology.

AUTHOR CONTRIBUTIONS

G.E.C. and A.S. conceived and designed the study; G.E.C. carried out experiments and analyzed and interpreted data; E.C. conducted all experiments during the revision process. A.D. assisted with mouse breeding and screening; P.Z. and D.B. performed computational analyses; A. Scrivo conducted microscopy analyses. For human study: B.M.B., H.S.L., and M.D.H. conceptualized the study; S.W.K., H.J.J., H.S.L., and B.M.B carried out data curation, analyses, visualization, and methodology; G.E.C. and A.S. wrote the manuscript, with all authors contributing to the writing and providing feedback.

DECLARATION OF INTERESTS

M.D.H. is currently an employee and shareholder at AstraZeneca. M.D.H. current address: Early Clinical Development, Oncology R&D, AstraZeneca, New York, NY, USA. B.M.B. received funding from AstaZeneca for the clinical trial related to this project, clinical trial funding from Momatero-Gene, clinical trial funding from Novartis.

Received: July 1, 2023
Revised: March 11, 2024
Accepted: May 29, 2024
Published: June 20, 2024

REFERENCES

1. Philip, M., and Schietinger, A. (2022). CD8(+) T cell differentiation and dysfunction in cancer. Nat. Rev. Immunol. *22*, 209–223. https://doi.org/10.1038/s41577-021-00574-3.
2. Anderson, K.G., Stromnes, I.M., and Greenberg, P.D. (2017). Obstacles Posed by the Tumor Microenvironment to T cell Activity: A Case for Synergistic Therapies. Cancer Cell *31*, 311–325. https://doi.org/10.1016/j.ccell.2017.02.008.
3. Gajewski, T.F., Schreiber, H., and Fu, Y.X. (2013). Innate and adaptive immune cells in the tumor microenvironment. Nat. Immunol. *14*, 1014–1022. https://doi.org/10.1038/ni.2703.

4. Yang, J.C., and Rosenberg, S.A. (2016). Adoptive T-Cell Therapy for Cancer. Adv. Immunol. *130*, 279–294. https://doi.org/10.1016/bs.ai.2015.12.006.

5. Leko, V., and Rosenberg, S.A. (2020). Identifying and Targeting Human Tumor Antigens for T Cell-Based Immunotherapy of Solid Tumors. Cancer Cell *38*, 454–472. https://doi.org/10.1016/j.ccell.2020.07.013.

6. Schmitt, T.M., Stromnes, I.M., Chapuis, A.G., and Greenberg, P.D. (2015). New Strategies in Engineering T-cell Receptor Gene-Modified T cells to More Effectively Target Malignancies. Clin. Cancer Res. *21*, 5191–5197. https://doi.org/10.1158/1078-0432.CCR-15-0860.

7. Rosenberg, S.A., Aebersold, P., Cornetta, K., Kasid, A., Morgan, R.A., Moen, R., Karson, E.M., Lotze, M.T., Yang, J.C., Topalian, S.L., et al. (1990). Gene transfer into humans–immunotherapy of patients with advanced melanoma, using tumor-infiltrating lymphocytes modified by retroviral gene transduction. N. Engl. J. Med. *323*, 570–578. https://doi.org/10.1056/NEJM199008303230904.

8. Schmitt, T.M., Ragnarsson, G.B., and Greenberg, P.D. (2009). T cell receptor gene therapy for cancer. Hum. Gene Ther. *20*, 1240–1248. https://doi.org/10.1089/hum.2009.146.

9. Morgan, R.A., Dudley, M.E., Wunderlich, J.R., Hughes, M.S., Yang, J.C., Sherry, R.M., Royal, R.E., Topalian, S.L., Kammula, U.S., Restifo, N.P., et al. (2006). Cancer regression in patients after transfer of genetically engineered lymphocytes. Science *314*, 126–129. https://doi.org/10.1126/science.1129003.

10. Morgan, R.A., Dudley, M.E., and Rosenberg, S.A. (2010). Adoptive cell therapy: genetic modification to redirect effector cell specificity. Cancer J. *16*, 336–341. https://doi.org/10.1097/PPO.0b013e3181eb3879.

11. Rosenberg, S.A., and Dudley, M.E. (2004). Cancer regression in patients with metastatic melanoma after the transfer of autologous antitumor lymphocytes. Proc. Natl. Acad. Sci. USA *101*, 14639–14645. https://doi.org/10.1073/pnas.0405730101.

12. Rosenberg, S.A., Yang, J.C., Sherry, R.M., Kammula, U.S., Hughes, M.S., Phan, G.Q., Citrin, D.E., Restifo, N.P., Robbins, P.F., Wunderlich, J.R., et al. (2011). Durable complete responses in heavily pretreated patients with metastatic melanoma using T-cell transfer immunotherapy. Clin. Cancer Res. *17*, 4550–4557. https://doi.org/10.1158/1078-0432.CCR-11-0116.

13. Yee, C., Thompson, J.A., Byrd, D., Riddell, S.R., Roche, P., Celis, E., and Greenberg, P.D. (2002). Adoptive T cell therapy using antigen-specific CD8+ T cell clones for the treatment of patients with metastatic melanoma: *in vivo* persistence, migration, and antitumor effect of transferred T cells. Proc. Natl. Acad. Sci. USA *99*, 16168–16173. https://doi.org/10.1073/pnas.242600099.

14. Chapuis, A.G., Egan, D.N., Bar, M., Schmitt, T.M., McAfee, M.S., Paulson, K.G., Voillet, V., Gottardo, R., Ragnarsson, G.B., Bleakley, M., et al. (2019). T cell receptor gene therapy targeting WT1 prevents acute myeloid leukemia relapse post-transplant. Nat. Med. *25*, 1064–1072. https://doi.org/10.1038/s41591-019-0472-9.

15. Dudley, M.E., Wunderlich, J.R., Robbins, P.F., Yang, J.C., Hwu, P., Schwartzentruber, D.J., Topalian, S.L., Sherry, R., Restifo, N.P., Hubicki, A.M., et al. (2002). Cancer regression and autoimmunity in patients after clonal repopulation with antitumor lymphocytes. Science *298*, 850–854. https://doi.org/10.1126/science.1076514.

16. Stromnes, I.M., Schmitt, T.M., Hulbert, A., Brockenbrough, J.S., Nguyen, H., Cuevas, C., Dotson, A.M., Tan, X., Hotes, J.L., Greenberg, P.D., et al. (2015). T Cells Engineered against a Native Antigen Can Surmount Immunologic and Physical Barriers to Treat Pancreatic Ductal Adenocarcinoma. Cancer Cell *28*, 638–652. https://doi.org/10.1016/j.ccell.2015.09.022.

17. Leen, A.M., Rooney, C.M., and Foster, A.E. (2007). Improving T cell therapy for cancer. Annu. Rev. Immunol. *25*, 243–265. https://doi.org/10.1146/annurev.immunol.25.022106.141527.

18. Wrzesinski, C., Paulos, C.M., Kaiser, A., Muranski, P., Palmer, D.C., Gattinoni, L., Yu, Z., Rosenberg, S.A., and Restifo, N.P. (2010). Increased intensity lymphodepletion enhances tumor treatment efficacy of adoptively transferred tumor-specific T cells. J. Immunother. *33*, 1–7. https://doi.org/10.1097/CJI.0b013e3181b88ffc.

19. Klebanoff, C.A., Khong, H.T., Antony, P.A., Palmer, D.C., and Restifo, N.P. (2005). Sinks, suppressors and antigen presenters: how lymphodepletion enhances T cell-mediated tumor immunotherapy. Trends Immunol. *26*, 111–117. https://doi.org/10.1016/j.it.2004.12.003.

20. Klebanoff, C.A., Finkelstein, S.E., Surman, D.R., Lichtman, M.K., Gattinoni, L., Theoret, M.R., Grewal, N., Spiess, P.J., Antony, P.A., Palmer, D.C., et al. (2004). IL-15 enhances the *in vivo* antitumor activity of tumor-reactive CD8+ T cells. Proc. Natl. Acad. Sci. USA *101*, 1969–1974. https://doi.org/10.1073/pnas.0307298101.

21. Restifo, N.P., Dudley, M.E., and Rosenberg, S.A. (2012). Adoptive immunotherapy for cancer: harnessing the T cell response. Nat. Rev. Immunol. *12*, 269–281. https://doi.org/10.1038/nri3191.

22. Baulu, E., Gardet, C., Chuvin, N., and Depil, S. (2023). TCR-engineered T cell therapy in solid tumors: State of the art and perspectives. Sci. Adv. *9*, eadf3700. https://doi.org/10.1126/sciadv.adf3700.

23. Chandran, S.S., and Klebanoff, C.A. (2019). T cell receptor-based cancer immunotherapy: Emerging efficacy and pathways of resistance. Immunol. Rev. *290*, 127–147. https://doi.org/10.1111/imr.12772.

24. Borst, J., Ahrends, T., Bąbała, N., Melief, C.J.M., and Kastenmüller, W. (2018). CD4(+) T cell help in cancer immunology and immunotherapy. Nat. Rev. Immunol. *18*, 635–647. https://doi.org/10.1038/s41577-018-0044-0.

25. Bennett, S.R., Carbone, F.R., Karamalis, F., Flavell, R.A., Miller, J.F., and Heath, W.R. (1998). Help for cytotoxic-T-cell responses is mediated by CD40 signalling. Nature *393*, 478–480. https://doi.org/10.1038/30996.

26. Schoenberger, S.P., Toes, R.E., van der Voort, E.I., Offringa, R., and Melief, C.J. (1998). T-cell help for cytotoxic T lymphocytes is mediated by CD40-CD40L interactions. Nature *393*, 480–483. https://doi.org/10.1038/31002.

27. Ridge, J.P., Di Rosa, F., and Matzinger, P. (1998). A conditioned dendritic cell can be a temporal bridge between a CD4+ T-helper and a T-killer cell. Nature *393*, 474–478. https://doi.org/10.1038/30989.

28. Castellino, F., Huang, A.Y., Altan-Bonnet, G., Stoll, S., Scheinecker, C., and Germain, R.N. (2006). Chemokines enhance immunity by guiding naive CD8+ T cells to sites of CD4+ T cell-dendritic cell interaction. Nature *440*, 890–895. https://doi.org/10.1038/nature04651.

29. Castellino, F., and Germain, R.N. (2006). Cooperation between CD4+ and CD8+ T cells: when, where, and how. Annu. Rev. Immunol. *24*, 519–540. https://doi.org/10.1146/annurev.immunol.23.021704.115825.

30. Le Saout, C., Mennechet, S., Taylor, N., and Hernandez, J. (2008). Memory-like CD8+ and CD4+ T cells cooperate to break peripheral tolerance under lymphopenic conditions. Proc. Natl. Acad. Sci. USA *105*, 19414–19419. https://doi.org/10.1073/pnas.0807743105.

31. Nakanishi, Y., Lu, B., Gerard, C., and Iwasaki, A. (2009). CD8(+) T lymphocyte mobilization to virus-infected tissue requires CD4(+) T-cell help. Nature *462*, 510–513. https://doi.org/10.1038/nature08511.

32. Bos, R., and Sherman, L.A. (2010). CD4+ T-cell help in the tumor milieu is required for recruitment and cytolytic function of CD8+ T lymphocytes. Cancer Res. *70*, 8368–8377. https://doi.org/10.1158/0008-5472.CAN-10-1322.

33. Greenberg, P.D., Kern, D.E., and Cheever, M.A. (1985). Therapy of disseminated murine leukemia with cyclophosphamide and immune Lyt-1+,2- T cells. Tumor eradication does not require participation of cytotoxic T cells. J. Exp. Med. *161*, 1122–1134.

34. Frey, A.B. (1995). Rat mammary adenocarcinoma 13762 expressing IFN-gamma elicits antitumor CD4+ MHC class II-restricted T cells that are cytolytic *in vitro* and tumoricidal *in vivo*. J. Immunol. *154*, 4613–4622.

35. Mumberg, D., Monach, P.A., Wanderling, S., Philip, M., Toledano, A.Y., Schreiber, R.D., and Schreiber, H. (1999). CD4(+) T cells eliminate MHC class II-negative cancer cells *in vivo* by indirect effects of IFN-gamma. Proc. Natl. Acad. Sci. USA *96*, 8633–8638.

36. Monach, P.A., Meredith, S.C., Siegel, C.T., and Schreiber, H. (1995). A unique tumor antigen produced by a single amino acid substitution. Immunity *2*, 45–59.

37. Perez-Diez, A., Joncker, N.T., Choi, K., Chan, W.F.N., Anderson, C.C., Lantz, O., and Matzinger, P. (2007). CD4 cells can be more efficient at tumor rejection than CD8 cells. Blood *109*, 5346–5354. https://doi.org/10.1182/blood-2006-10-051318.

38. Qin, Z., and Blankenstein, T. (2000). CD4+ T cell–mediated tumor rejection involves inhibition of angiogenesis that is dependent on IFN gamma receptor expression by nonhematopoietic cells. Immunity *12*, 677–686. https://doi.org/10.1016/s1074-7613(00)80218-6.

39. Egilmez, N.K., Hess, S.D., Chen, F.A., Takita, H., Conway, T.F., and Bankert, R.B. (2002). Human CD4+ effector T cells mediate indirect interleukin-12- and interferon-gamma-dependent suppression of autologous HLA-negative lung tumor xenografts in severe combined immunodeficient mice. Cancer Res. *62*, 2611–2617.

40. Broderick, L., Yokota, S.J., Reineke, J., Mathiowitz, E., Stewart, C.C., Barcos, M., Kelleher, R.J., Jr., and Bankert, R.B. (2005). Human CD4+ effector memory T cells persisting in the microenvironment of lung cancer xenografts are activated by local delivery of IL-12 to proliferate, produce IFN-gamma, and eradicate tumor cells. J. Immunol. *174*, 898–906. https://doi.org/10.4049/jimmunol.174.2.898.

41. Muranski, P., Boni, A., Antony, P.A., Cassard, L., Irvine, K.R., Kaiser, A., Paulos, C.M., Palmer, D.C., Touloukian, C.E., Ptak, K., et al. (2008). Tumor-specific Th17-polarized cells eradicate large established melanoma. Blood *112*, 362–373. https://doi.org/10.1182/blood-2007-11-120998.

42. Greenberg, P.D. (1991). Adoptive T cell therapy of tumors: mechanisms operative in the recognition and elimination of tumor cells. Adv. Immunol. *49*, 281–355. https://doi.org/10.1016/s0065-2776(08)60778-6.

43. Hung, K., Hayashi, R., Lafond-Walker, A., Lowenstein, C., Pardoll, D., and Levitsky, H. (1998). The central role of CD4(+) T cells in the antitumor immune response. J. Exp. Med. *188*, 2357–2368. https://doi.org/10.1084/jem.188.12.2357.

44. Braumuller, H., Wieder, T., Brenner, E., Assmann, S., Hahn, M., Alkhaled, M., Schilbach, K., Essmann, F., Kneilling, M., Griessinger, C., et al. (2013). T-helper-1-cell cytokines drive cancer into senescence. Nature *494*, 361–365. https://doi.org/10.1038/nature11824.

45. Muller-Hermelink, N., Braumuller, H., Pichler, B., Wieder, T., Mailhammer, R., Schaak, K., Ghoreschi, K., Yazdi, A., Haubner, R., Sander, C.A., et al. (2008). TNFR1 signaling and IFN-gamma signaling determine whether T cells induce tumor dormancy or promote multistage carcinogenesis. Cancer Cell *13*, 507–518. https://doi.org/10.1016/j.ccr.2008.04.001.

46. Schietinger, A., Philip, M., Liu, R.B., Schreiber, K., and Schreiber, H. (2010). Bystander killing of cancer requires the cooperation of CD4(+) and CD8(+) T cells during the effector phase. J. Exp. Med. *207*, 2469–2477. https://doi.org/10.1084/jem.20092450.

47. Espinosa-Carrasco, G., Le Saout, C., Fontanaud, P., Stratmann, T., Mollard, P., Schaeffer, M., and Hernandez, J. (2017). CD4(+) T Helper Cells Play a Key Role in Maintaining Diabetogenic CD8(+) T Cell Function in the Pancreas. Front. Immunol. *8*, 2001. https://doi.org/10.3389/fimmu.2017.02001.

48. Alspach, E., Lussier, D.M., Miceli, A.P., Kizhvatov, I., DuPage, M., Luoma, A.M., Meng, W., Lichti, C.F., Esaulova, E., Vomund, A.N., et al. (2019). MHC-II neoantigens shape tumour immunity and response to immunotherapy. Nature *574*, 696–701. https://doi.org/10.1038/s41586-019-1671-8.

49. Sahin, U., Derhovanessian, E., Miller, M., Kloke, B.P., Simon, P., Löwer, M., Bukur, V., Tadmor, A.D., Luxemburger, U., Schrörs, B., et al. (2017). Personalized RNA mutanome vaccines mobilize poly-specific therapeutic immunity against cancer. Nature *547*, 222–226. https://doi.org/10.1038/nature23003.

50. Ott, P.A., Hu, Z., Keskin, D.B., Shukla, S.A., Sun, J., Bozym, D.J., Zhang, W., Luoma, A., Giobbie-Hurder, A., Peter, L., et al. (2017). An immunogenic personal neoantigen vaccine for patients with melanoma. Nature *547*, 217–221. https://doi.org/10.1038/nature22991.

51. Tran, E., Turcotte, S., Gros, A., Robbins, P.F., Lu, Y.C., Dudley, M.E., Wunderlich, J.R., Somerville, R.P., Hogan, K., Hinrichs, C.S., et al. (2014). Cancer immunotherapy based on mutation-specific CD4+ T cells in a patient with epithelial cancer. Science *344*, 641–645. https://doi.org/10.1126/science.1251102.

52. Hunder, N.N., Wallen, H., Cao, J., Hendricks, D.W., Reilly, J.Z., Rodmyre, R., Jungbluth, A., Gnjatic, S., Thompson, J.A., and Yee, C. (2008). Treatment of metastatic melanoma with autologous CD4+ T cells against NY-ESO-1. N. Engl. J. Med. *358*, 2698–2703. https://doi.org/10.1056/NEJMoa0800251.

53. Greenberg, P.D., Cheever, M.A., and Fefer, A. (1981). Eradication of disseminated murine leukemia by chemoimmunotherapy with cyclophosphamide and adoptively transferred immune syngeneic Lyt-1+2- lymphocytes. J. Exp. Med. *154*, 952–963.

54. Gattinoni, L., Finkelstein, S.E., Klebanoff, C.A., Antony, P.A., Palmer, D.C., Spiess, P.J., Hwang, L.N., Yu, Z., Wrzesinski, C., Heimann, D.M., et al. (2005). Removal of homeostatic cytokine sinks by lymphodepletion enhances the efficacy of adoptively transferred tumor-specific CD8+ T cells. J. Exp. Med. *202*, 907–912. https://doi.org/10.1084/jem.20050732.

55. Scott, A.C., Dündar, F., Zumbo, P., Chandran, S.S., Klebanoff, C.A., Shakiba, M., Trivedi, P., Menocal, L., Appleby, H., Camara, S., et al. (2019). TOX is a critical regulator of tumour-specific T cell differentiation. Nature *571*, 270–274. https://doi.org/10.1038/s41586-019-1324-y.

56. Kim, K., Park, S., Park, S.Y., Kim, G., Park, S.M., Cho, J.W., Kim, D.H., Park, Y.M., Koh, Y.W., Kim, H.R., et al. (2020). Single-cell transcriptome analysis reveals TOX as a promoting factor for T cell exhaustion and a predictor for anti-PD-1 responses in human cancer. Genome Med. *12*, 22. https://doi.org/10.1186/s13073-020-00722-9.

57. Seo, H., Chen, J., González-Avalos, E., Samaniego-Castruita, D., Das, A., Wang, Y.H., López-Moyado, I.F., Georges, R.O., Zhang, W., Onodera, A., et al. (2019). TOX and TOX2 transcription factors cooperate with NR4A transcription factors to impose CD8(+) T cell exhaustion. Proc. Natl. Acad. Sci. USA *116*, 12410–12415. https://doi.org/10.1073/pnas.1905675116.

58. Wang, X., He, Q., Shen, H., Xia, A., Tian, W., Yu, W., and Sun, B. (2019). TOX promotes the exhaustion of antitumor CD8(+) T cells by preventing PD1 degradation in hepatocellular carcinoma. J. Hepatol. *71*, 731–741. https://doi.org/10.1016/j.jhep.2019.05.015.

59. Khan, O., Giles, J.R., McDonald, S., Manne, S., Ngiow, S.F., Patel, K.P., Werner, M.T., Huang, A.C., Alexander, K.A., Wu, J.E., et al. (2019). TOX transcriptionally and epigenetically programs CD8(+) T cell exhaustion. Nature *571*, 211–218. https://doi.org/10.1038/s41586-019-1325-x.

60. Alfei, F., Kanev, K., Hofmann, M., Wu, M., Ghoneim, H.E., Roelli, P., Utzschneider, D.T., von Hoesslin, M., Cullen, J.G., Fan, Y., et al. (2019). TOX reinforces the phenotype and longevity of exhausted T cells in chronic viral infection. Nature *571*, 265–269. https://doi.org/10.1038/s41586-019-1326-9.

61. Wu, M., Fang, H., and Hwang, S.T. (2001). Cutting edge: CCR4 mediates antigen-primed T cell binding to activated dendritic cells. J. Immunol. *167*, 4791–4795. https://doi.org/10.4049/jimmunol.167.9.4791.

62. Krishna, S., Lowery, F.J., Copeland, A.R., Bahadiroglu, E., Mukherjee, R., Jia, L., Anibal, J.T., Sachs, A., Adebola, S.O., Gurusamy, D., et al. (2020). Stem-like CD8 T cells mediate response of adoptive cell immunotherapy against human cancer. Science *370*, 1328–1334. https://doi.org/10.1126/science.abb9847.

63. Jung, S., Unutmaz, D., Wong, P., Sano, G.I., De los Santos, K., Sparwasser, T., Wu, S., Vuthoori, S., Ko, K., Zavala, F., et al. (2002). In vivo depletion of CD11c+ dendritic cells abrogates priming of CD8+ T cells by exogenous cell-associated antigens. Immunity *17*, 211–220. https://doi.org/10.1016/s1074-7613(02)00365-5.

64. Mitchison, N.A., and O'Malley, C. (1987). Three-cell-type clusters of T cells with antigen-presenting cells best explain the epitope linkage

and noncognate requirements of the *in vivo* cytolytic response. Eur. J. Immunol. *17*, 1579–1583. https://doi.org/10.1002/eji.1830171109.

65. Baumeister, S.H., Freeman, G.J., Dranoff, G., and Sharpe, A.H. (2016). Coinhibitory Pathways in Immunotherapy for Cancer. Annu. Rev. Immunol. *34*, 539–573. https://doi.org/10.1146/annurev-immunol-032414-112049.
66. Haslam, A., and Prasad, V. (2019). Estimation of the Percentage of US Patients With Cancer Who Are Eligible for and Respond to Checkpoint Inhibitor Immunotherapy Drugs. JAMA Netw. Open *2*, e192535. https://doi.org/10.1001/jamanetworkopen.2019.2535.
67. Kalbasi, A., and Ribas, A. (2020). Tumour-intrinsic resistance to immune checkpoint blockade. Nat. Rev. Immunol. *20*, 25–39. https://doi.org/10.1038/s41577-019-0218-4.
68. Fares, C.M., Van Allen, E.M., Drake, C.G., Allison, J.P., and Hu-Lieskovan, S. (2019). Mechanisms of Resistance to Immune Checkpoint Blockade: Why Does Checkpoint Inhibitor Immunotherapy Not Work for All Patients? Am. Soc. Clin. Oncol. Educ. Book. *39*, 147–164. https://doi.org/10.1200/EDBK_240837.
69. Lee, H.S., Jang, H.J., Ramineni, M., Wang, D.Y., Ramos, D., Choi, J.M., Splawn, T., Espinoza, M., Almarez, M., Hosey, L., et al. (2023). A Phase II Window of Opportunity Study of Neoadjuvant PD-L1 versus PD-L1 plus CTLA-4 Blockade for Patients with Malignant Pleural Mesothelioma. Clin. Cancer Res. *29*, 548–559. https://doi.org/10.1158/1078-0432.CCR-22-2566.
70. Keene, J.A., and Forman, J. (1982). Helper activity is required for the *in vivo* generation of cytotoxic T lymphocytes. J. Exp. Med. *155*, 768–782. https://doi.org/10.1084/jem.155.3.768.
71. Hu, H.M., Winter, H., Urba, W.J., and Fox, B.A. (2000). Divergent roles for CD4+ T cells in the priming and effector/memory phases of adoptive immunotherapy. J. Immunol. *165*, 4246–4253. https://doi.org/10.4049/jimmunol.165.8.4246.
72. Gao, F.G., Khammanivong, V., Liu, W.J., Leggatt, G.R., Frazer, I.H., and Fernando, G.J.P. (2002). Antigen-specific CD4+ T-cell help is required to activate a memory CD8+ T cell to a fully functional tumor killer cell. Cancer Res. *62*, 6438–6441.
73. Shirai, M., Pendleton, C.D., Ahlers, J., Takeshita, T., Newman, M., and Berzofsky, J.A. (1994). Helper-cytotoxic T lymphocyte (CTL) determinant linkage required for priming of anti-HIV CD8+ CTL *in vivo* with peptide vaccine constructs. J. Immunol. *152*, 549–556.
74. Dolina, J.S., Lee, J., Brightman, S.E., McArdle, S., Hall, S.M., Thota, R.R., Zavala, K.S., Lanka, M., Ramamoorthy Premlal, A.L., Greenbaum, J.A., et al. (2023). Linked CD4+/CD8+ T cell neoantigen vaccination overcomes immune checkpoint blockade resistance and enables tumor regression. J. Clin. Invest. *133*, e164258. https://doi.org/10.1172/JCI164258.
75. Melief, C.J.M., and van der Burg, S.H. (2008). Immunotherapy of established (pre)malignant disease by synthetic long peptide vaccines. Nat. Rev. Cancer *8*, 351–360. https://doi.org/10.1038/nrc2373.
76. Magen, A., Hamon, P., Fiaschi, N., Soong, B.Y., Park, M.D., Mattiuz, R., Humblin, E., Troncoso, L., D'Souza, D., Dawson, T., et al. (2023). Intratumoral dendritic cell-CD4(+) T helper cell niches enable CD8(+) T cell differentiation following PD-1 blockade in hepatocellular carcinoma. Nat. Med. *29*, 1389–1399. https://doi.org/10.1038/s41591-023-02345-0.
77. Schietinger, A., Arina, A., Liu, R.B., Wells, S., Huang, J., Engels, B., Bindokas, V., Bartkowiak, T., Lee, D., Herrmann, A., et al. (2013). Longitudinal confocal microscopy imaging of solid tumor destruction following adoptive T cell transfer. Oncoimmunology *2*, e26677. https://doi.org/10.4161/onci.26677.
78. Shakiba, M., Zumbo, P., Espinosa-Carrasco, G., Menocal, L., Dündar, F., Carson, S.E., Bruno, E.M., Sanchez-Rivera, F.J., Lowe, S.W., Camara, S., et al. (2022). TCR signal strength defines distinct mechanisms of T cell dysfunction and cancer evasion. J. Exp. Med. *219*, e20201966. https://doi.org/10.1084/jem.20201966.
79. Dobin, A., Davis, C.A., Schlesinger, F., Drenkow, J., Zaleski, C., Jha, S., Batut, P., Chaisson, M., and Gingeras, T.R. (2013). STAR: ultrafast universal RNA-seq aligner. Bioinformatics *29*, 15–21. https://doi.org/10.1093/bioinformatics/bts635.
80. Liao, Y., Smyth, G.K., and Shi, W. (2014). featureCounts: an efficient general purpose program for assigning sequence reads to genomic features. Bioinformatics *30*, 923–930. https://doi.org/10.1093/bioinformatics/btt656.
81. Love, M.I., Huber, W., and Anders, S. (2014). Moderated estimation of fold change and dispersion for RNA-seq data with DESeq2. Genome Biol. *15*, 550. https://doi.org/10.1186/s13059-014-0550-8.
82. Korotkevich, G., Sukhov, V., Budin, N., Shpak, B., Artyomov, M.N., and Sergushichev, A. (2021). Fast gene set enrichment analysis. Preprint at bioRxiv. https://doi.org/10.1101/060012.
83. Yu, G., Wang, L.G., Han, Y., and He, Q.Y. (2012). clusterProfiler: an R package for comparing biological themes among gene clusters. OMICS *16*, 284–287. https://doi.org/10.1089/omi.2011.0118.
84. Li, H., and Durbin, R. (2009). Fast and accurate short read alignment with Burrows-Wheeler transform. Bioinformatics *25*, 1754–1760. https://doi.org/10.1093/bioinformatics/btp324.
85. Danecek, P., Bonfield, J.K., Liddle, J., Marshall, J., Ohan, V., Pollard, M.O., Whitwham, A., Keane, T., McCarthy, S.A., Davies, R.M., et al. (2021). Twelve years of SAMtools and BCFtools. GigaScience *10*, giab008. https://doi.org/10.1093/gigascience/giab008.
86. Zhang, Y., Liu, T., Meyer, C.A., Eeckhoute, J., Johnson, D.S., Bernstein, B.E., Nusbaum, C., Myers, R.M., Brown, M., Li, W., et al. (2008). Model-based analysis of ChIP-Seq (MACS). Genome Biol. *9*, R137. https://doi.org/10.1186/gb-2008-9-9-r137.
87. Stark, R., and Brown, G. (2011). DiffBind: differential binding analysis of ChIP-Seq peak data. http://bioconductor.org/packages/release/bioc/vignettes/DiffBind/inst/doc/DiffBind.pdf.
88. Wang, Q., Li, M., Wu, T., Zhan, L., Li, L., Chen, M., Xie, W., Xie, Z., Hu, E., Xu, S., et al. (2022). Exploring Epigenomic Datasets by ChIPseeker. Curr. Protoc. *2*, e585. https://doi.org/10.1002/cpz1.585.
89. Ramirez, F., Dundar, F., Diehl, S., Gruning, B.A., and Manke, T. (2014). deepTools: a flexible platform for exploring deep-sequencing data. Nucleic Acids Res. *42*, W187–W191. https://doi.org/10.1093/nar/gku365.
90. Kuhn, R.M., Haussler, D., and Kent, W.J. (2013). The UCSC genome browser and associated tools. Brief. Bioinform. *14*, 144–161. https://doi.org/10.1093/bib/bbs038.
91. Robinson, J.T., Thorvaldsdottir, H., Winckler, W., Guttman, M., Lander, E.S., Getz, G., and Mesirov, J.P. (2011). Integrative genomics viewer. Nat. Biotechnol. *29*, 24–26. https://doi.org/10.1038/nbt.1754.
92. Carroll, T., and Barrows, D. (2023). profileplyr: Visualization and annotation of read signal over genomic ranges with profileplyr (R package).
93. Heinz, S., Benner, C., Spann, N., Bertolino, E., Lin, Y.C., Laslo, P., Cheng, J.X., Murre, C., Singh, H., and Glass, C.K. (2010). Simple combinations of lineage-determining transcription factors prime cis-regulatory elements required for macrophage and B cell identities. Mol. Cell *38*, 576–589. https://doi.org/10.1016/j.molcel.2010.05.004.
94. Wu, T., Hu, E., Xu, S., Chen, M., Guo, P., Dai, Z., Feng, T., Zhou, L., Tang, W., Zhan, L., et al. (2021). clusterProfiler 4.0: A universal enrichment tool for interpreting omics data. Innovation *2*, 100141. https://doi.org/10.1016/j.xinn.2021.100141.
95. Yu, G., Wang, L.G., and He, Q.Y. (2015). ChIPseeker: an R/Bioconductor package for ChIP peak annotation, comparison and visualization. Bioinformatics *31*, 2382–2383. https://doi.org/10.1093/bioinformatics/btv145.
96. Gu, Z., Eils, R., and Schlesner, M. (2016). Complex heatmaps reveal patterns and correlations in multidimensional genomic data. Bioinformatics *32*, 2847–2849. https://doi.org/10.1093/bioinformatics/btw313.
97. Berg, S., Kutra, D., Kroeger, T., Straehle, C.N., Kausler, B.X., Haubold, C., Schiegg, M., Ales, J., Beier, T., Rudy, M., et al. (2019).

ilastik: interactive machine learning for (bio)image analysis. Nat. Methods *16*, 1226–1232. https://doi.org/10.1038/s41592-019-0582-9.

98. Greenwald, N.F., Miller, G., Moen, E., Kong, A., Kagel, A., Dougherty, T., Fullaway, C.C., McIntosh, B.J., Leow, K.X., Schwartz, M.S., et al. (2022). Whole-cell segmentation of tissue images with human-level performance using large-scale data annotation and deep learning. Nat. Biotechnol. *40*, 555–565. https://doi.org/10.1038/s41587-021-01094-0.

99. Giesen, C., Wang, H.A.O., Schapiro, D., Zivanovic, N., Jacobs, A., Hattendorf, B., Schüffler, P.J., Grolimund, D., Buhmann, J.M., Brandt, S., et al. (2014). Highly multiplexed imaging of tumor tissues with subcellular resolution by mass cytometry. Nat. Methods *11*, 417–422. https://doi.org/10.1038/nmeth.2869.

100. Wolf, F.A., Angerer, P., and Theis, F.J. (2018). SCANPY: large-scale single-cell gene expression data analysis. Genome Biol. *19*, 15. https://doi.org/10.1186/s13059-017-1382-0.

STAR★METHODS

KEY RESOURCES TABLE

REAGENT or RESOURCE	SOURCE	IDENTIFIER
Antibodies		
APC anti-mouse IFN-γ (clone XMG1.2)	Biolegend	Cat#: 505810
PE/Cyanine7 anti-mouse TNF-α (clone MP6-XT22)	Biolegend	Cat#: 506324
PE-CF594 anti-human Granzyme B (clone GB11)	BD Bioscience	Cat#: 562462
FITC anti-mouse CD107a (clone 1D4B)	BD Bioscience	Cat#: 553793
FITC anti-mouse CD107b (clone ABL-93)	BD Bioscience	Cat#: 558758
BUV737 anti-mouse CD4 (clone RM4-5)	BD Bioscience	Cat#: 612843
BV711 anti-mouse CD70 (clone FR70)	BD Bioscience	Cat#: 740741
Brilliant Violet 650 anti-mouse CD8a (clone53–6.7)	Biolegend	Cat#: 100742
Alexa Fluor 700 anti-mouse I-A/I-E (clone M5/114.15.2)	Biolegend	Cat#: 107622
PE/Cyanine7 anti-mouse CD11c (clone N418)	Biolegend	Cat#: 117318
FITC anti-mouse CD86 (clone GL-1)	Biolegend	Cat#: 105006
APC/Cyanine7 anti-mouse CD27 (clone LG.3A10)	Biolegend	Cat#: 124226
PE/Cyanine7 anti-T-bet (clone 4B10)	Biolegend	Cat#: 644824
PerCP/Cyanine5.5 anti-mouse CD279 (clone RMP1-30)	Biolegend	Cat#: 109120
Brilliant Violet 421 anti-mouse CD45.1 (clone A20)	Biolegend	Cat#: 110732
Brilliant Violet 711 anti-rat mouse CD90.1 (clone OX-7)	Biolegend	Cat#: 202539
PE anti-mouse CD223 (LAG-3) (clone C9B7W)	Biolegend	Cat#: 125207
APC anti-mouse CD366 (Tim3) (clone RMT3-23)	Biolegend	Cat#: 119706
Alexa Fluor 647 anti-mouse CD39 (clone Duha59)	Biolegend	Cat#: 143808
PE/Cyanine7 anti-mouse CD244.2 (2B4)(clone m2B 4458.1)	Biolegend	Cat#: 133512
Brilliant Violet 785 anti-mouse CD44 (clone IM7)	Biolegend	Cat#: 103059
PE anti-mouse CD40 (clone 1C10)	Invitrogen	Cat#: 12-0401-83
PE anti-mouse TOX (clone REA473)	Miltenyi Biotec	Cat#: 130-120-716
Brilliant Violet 421 anti-mouse CD90.2 (clone 30-H12)	Biolegend	Cat#: 105341
APC anti-mouse CD45.2 (clone 104)	Biolegend	Cat#: 109814
PE anti-Mouse Vα2 TCR (clone B20.1)	BD Bioscience	Cat#: 561078
PE anti-Mouse Vβ 8.1, 8.2 TCR (clone MR5-2)	BD Bioscience	Cat#: 553186
Anti-human IFN-γ 150ND	Standard BioTools	10761–890
Anti-human CD11c 154Sm (polyclonal)	Standard BioTools	3154025D
Anti-human FoxP3 155Gd (clone: 236A/E7)	Standard BioTools	3155016D
Anti-human CD4 156Gd (clone: EPR6855)	Standard BioTools	3156033D

(*Continued on next page*)

Continued

REAGENT or RESOURCE	SOURCE	IDENTIFIER
Anti-human CD8a 162Dy (clone: C8/144B)	Standard BioTools	3162034D
Anti-human Granzyme B 167Er (clone: EPR20129-217)	Standard BioTools	3167021D
Anti-human CD45RO 173Yb (clone: UCHL1)	Standard BioTools	3173016D
Anti-human PD-1 165Ho (clone: EPR4877(2))	Standard BioTools	3165039D
Bacterial and virus strains		
NEB 5-alpha Competent E. coli	New England Biolabs	Cat#: C2987H
Biological samples		
Patients' samples/tissues; Malignant Pleural Mesothelioma	from Lee H.S. et al.[69] and this paper	N/A
Chemicals, peptides, and recombinant proteins		
Cyclophosphamide	Amneal	Cat#: 70121-1240-1
IL-2	NIH	Cat#: RO 23-6019
InVivoMAb anti-mouse PD-1	BioXCell	Cat#: BE1046
InVivoMAb anti-mouse PD-L1	BioXCell	Cat#: BE0101
InVivoMAb anti-mouse CD4	BioXCell	Cat#: BE0003-1
OVA 257–264 peptide SIINFEKL	GeneScript	Cat#: N/A
GP 61–80 peptide GLKGPDIYKGVYQFKSVEFD	GeneScript	Cat#: N/A
RPMI 1640	Corning	Cat#: 10-041-CV
DMEM	Corning	Cat#: 10-013-CV
Fetal bovine serum	Corning	Cat#: 35-010-CV
Penicillin-streptomycin-Glutamine (100X)	Gibco	Cat#: 10378016
L-Glutamine (200mM)	Gibco	Cat#: A2916801
β-mercaptoethanol	Gibco	Cat#: 21985023
LIVE/DEAD Fixable blue Dead Cell Stain Kit	Thermo Fisher Scientific	Cat#: L34962
GolgiPlug Protein Transport Inhibitor	BD Bioscience	Cat#: 555029
RBC Lysis Buffer (10X)	Tonbo	Cat#: TNB-4300-L100
Lipofectamine 3000	Thermo Fisher Scientific	Cat#: L3000015
LB Broth Miller	Fisher	BP1426-500
Gibson Assembly Cloning Kit	New England Biolabs	Cat#: E5510S
Critical commercial assays		
Foxp3 fixation and permeabilization kit	Tonbo	Cat#: TNB-0607-KIT
CellTrace Violet Cell Proliferation Kit	Thermo Fisher Scientific	Cat#: C34571
Deposited data		
GSE265846 (RNA-seq)	This paper	GSE265846
GSE265847 (ATAC-seq)	This paper	GSE265847
Gene list of human $CD8^+$ TIL from Krishna et al.[62] used for GSEA in this paper.	Krishna et al.[62]	Table S6
Experimental models: Cell lines		
B16F10 (B16)	ATCC	Cat#: CRL-6475
MCA205 (MCA)	Dr. N. Restifo, NIH	N/A
Platinum E	Cell Biolabs, Inc.	Cat#: RV-101
Phoenix-AMPHO	ATCC	Cat#: CRL-3213
B16 OVA-GP (B16-OG)	This paper	N/A
B16 OVA (B16-O)	This paper	N/A
B16 GP (B16-G)	This paper	N/A
MCA205 OVA-GP (MCA-OG)	This paper	N/A

(*Continued on next page*)

Continued

REAGENT or RESOURCE	SOURCE	IDENTIFIER
Experimental models: Organisms/strains		
C57BL/6J (B6)	The Jackson Laboratory	Strain#: 000664
B6.PL-*Thy1*^{a}/CyJ (B6 Thy1.1)	The Jackson Laboratory	Strain#: 000406
B6.SJL-*Ptprc*^{a} *Pepc*^{b}/BoyJ (CD45.1)	The Jackson Laboratory	Strain#: 002014
B6.Cg-Tg(TcraTcrb)425Cbn/J (OT-II)	The Jackson Laboratory	Strain#: 004194
C57BL/6-Tg(TcraTcrb)1100Mjb/J (OT1)	The Jackson Laboratory	Strain#: 003831
B6.Cg-*Ptprc*^{a} *Pepc*^{b} Tg(TcrLCMV)1Aox/PpmJ (SMARTA)	The Jackson Laboratory	Strain#: 030450
B6.FVB-1700016L21RikTg(Itgax-HBEGF/EGFP)57Lan/J (CD11c-DTR)	The Jackson Laboratory	Strain#: 004509
B6.Cg-Tg(Itgax-Venus)1Mnz/J (CD11c-YFP)	The Jackson Laboratory	Strain#: 008829
Oligonucleotides		
EGFP_Fwd CTGGCTAGCATGGTGAGCA AGGGCGAG	IDT	N/A
EGFP_Rev GCCAGCTAGCTTACTTG TACAGCTCGTCC	IDT	N/A
CD11c YFP_Fwd TGCTGGTTGTTG TGCTGTCTCATC	IDT	N/A
CD11c YFP_Rev GGGGGTGTTCT GCTGGTAGTGGTC	IDT	N/A
DTR_Fwd GGG ACC ATG AAG CTG CTG CCG	IDT	N/A
DTR_Rev TCA GTG GGA ATT AGT CAT GCC	IDT	N/A
DTR WT_Fwd CCC TAT CTA GCT GCC CTC CT	IDT	N/A
DTR WT_Rev GGG GGA TGT AAT TGT GAA GGT	IDT	N/A
Recombinant DNA		
pMFG-EGFP	Schietinger et al., 2010[46]	N/A
pMFG-Cerulean	Schietinger et al., 2013[77]	N/A
tRFP retroviral vector	Shakiba et al., 2022[78]	N/A
Software and algorithms		
FACSDiva	BD Biosciences	N/A
FlowJo v 10.10	BD Biosciences	N/A
GraphPad PRISM 9 & 10	GraphPad Software	N/A
Fiji Is Just ImageJ (FIJI)	Fiji Software	
STAR v2.6.0c	Dobin et al., 2013[79]	https://github.com/alexdobin/STAR/releases
featureCounts (Subread v1.6.2)	Liao et al., 2014[80]	https://subread.sourceforge.net/featureCounts.html
R v4.1.0	R Core Team	https://cran.r-project.org
DESeq2 v1.34.0	Love et al., 2014[81]	https://bioconductor.org/packages/release/bioc/html/DESeq2.html
ggplot2 v3.4.1	Wickham	https://cran.r-project.org/web/packages/ggplot2/index.html
pheatmap v 1.0.12	Kolde	https://cran.r-project.org/web/packages/pheatmap/index.html
fgsea v1.20.0	Korotkevich et al., 2021[82]	https://bioconductor.org/packages/release/bioc/html/fgsea.html

(*Continued on next page*)

Continued

REAGENT or RESOURCE	SOURCE	IDENTIFIER
clusterProfiler v4.2.2	Yu et al., 2012[83]	https://bioconductor.org/packages/release/bioc/html/clusterProfiler.html
BWA v0.7.17	Li et al., 2009[84]	https://bio-bwa.sourceforge.net
samtools v1.8	Danecek et al., 2021[85]	http://www.htslib.org
Picard tools v2.18.9	Broad Institute	https://broadinstitute.github.io/picard/
MACS v2.1.1	Zhang et al., 2008[86]	https://github.com/macs3-project/MACS
DiffBind v3.4.11	Stark and Brown, 2011.[87]	https://bioconductor.org/packages/release/bioc/html/DiffBind.html
ChIPseeker v1.30.3	Wang et al., 2022[88]	https://www.bioconductor.org/packages/release/bioc/html/ChIPseeker.html
deepTools v3.1.0	Ramírez et al., 2014[89]	https://deeptools.readthedocs.io/en/develop/
bigWigMerge (UCSC KentUtils)	Kuhn et al., 2013[90]	https://github.com/ucscGenomeBrowser/kent
IGV	Robinson et al., 2011[91]	https://igv.org/doc/desktop/
profileplyr v1.10.2	Carroll and Barrows, 2023[92]	https://www.bioconductor.org/packages/release/bioc/html/profileplyr.html
ComplexHeatmap v2.15.1	Gu	https://bioconductor.org/packages/release/bioc/html/ComplexHeatmap.html
HOMER v4.10-0	Heinz et al., 2010[93]	http://homer.ucsd.edu/homer/motif/
marge v0.0.4	Amezquita	https://github.com/robertamezquita/marge

RESOURCE AVAILABILITY

Lead contact

Further information and requests for resources and reagents should be directed to and will be fulfilled by the lead contact, Andrea Schietinger (schietia@mskcc.org).

Materials availability

Plasmids and cell lines are available on request, but we may require completed Materials Transfer Agreement if there is potential for commercial application. Mouse lines used are all available at Jackson Lab, as listed in the key resources table.

Data and code availability

RNA-seq and ATAC-seq data have been deposited at GEO and are publicly available. Accession numbers are listed in the key resources table. Code has been deposited in GitHub. https://github.com/abcwcm/Espinosa-Carrasco2024. Any additional information required to reanalyze the data reported in this paper is available from the lead contact upon request.

EXPERIMENTAL MODEL AND STUDY PARTICIPANT DETAILS

Mice

B6 mice (C57BL/6J), TCR_{OT1} (C57BL/6-Tg(TcraTcrb)1100Mjb/J), TCR_{SMARTA} (B6.Cg-Ptprca Pepcb Tg(TcrLCMV)1Aox/PpmJ), CD11c-YFP (B6.Cg-Tg(Itgax-Venus)1Mnz/J), CD11c-DTR-GFP (B6.FVB-1700016L21RikTg(Itgax-DTR/EGFP)57Lan/J), GFP transgenic (C57BL/6-Tg(CAG-EGFP)1Osb/J), B6 Thy1.1 (B6.PL-Thy1a/CyJ), and B6 CD45.1 (B6.SJL-Ptprca Pepcb/BoyJ) mice were purchased from the Jackson Laboratory. TCR_{SMARTA} mice were crossed to Thy.1.1 mice to generate TCR_{SMARTA} Thy1.1 mice; for imaging studies, TCR_{SMARTA} Thy1.1 mice were crossed to GFP-transgenic mice to generate TCR_{SMARTA} Thy1.1 GFP mice. TCR_{OT1} (Thy1.2) mice were crossed to CD45.1 mice to generate TCR_{OT1} CD45.1 mice. Both female and male mice were used for experimental studies. Donor and host mice were age- and sex-matched; mice were 7–12 weeks old. All mice were bred and maintained in the animal facility at Memorial Sloan Kettering Cancer Center (MSKCC). Experiments were performed in compliance with the MSKCC Institutional Animal Care and Use Committee (IACUC) regulations.

Patient samples

For details on patients, study design, and methodology see Lee H.S. et al.[69] Briefly, this was a phase II, prospective, randomized window-of-opportunity trial completed at Baylor College of Medicine that enrolled patients with surgically resectable MPM (NCT02592551). Eligible patients underwent a staging procedure that included cervical mediastinoscopy with mediastinal lymph

node biopsies and diagnostic laparoscopy with peritoneal lavage and peritoneal biopsies. Thoracoscopy with tumor biopsies was performed for the purpose of the trial. Patients without pathologic nodal or peritoneal disease were randomly assigned in a 2:2:1 ratio to receive (i) one dose of durvalumab (10 mg/kg i.v.), (ii) one dose of durvalumab (1,500 mg) plus one dose of tremelimumab (75 mg i.v.), or (iii) no ICB. ICB was administered 3 days to 3 weeks following the staging procedure and surgical resection was performed 3 to 6 weeks after ICB by extended pleurectomy/decortication (P/D) or extrapleural pneumonectomy (EPP). Tumor and blood were obtained before and after ICB (at thoracoscopy and resection, respectively).

Cell lines

Phoenix packaging cell line and B16F10 mouse melanoma tumor cell line were purchased from ATCC. Platinum E cell line was purchased from Cell Biolabs. MCA205 cell line was a generous gift from N. Restifo (NIH). Cell lines were cultured in Dulbecco's Modified Eagle's Medium (DMEM) supplemented with 5–10% fetal bovine serum (FBS, Corning) and penicillin–streptomycin solution at 37C in a 5% CO2 humidified incubator.

METHOD DETAILS

Generation of plasmids and tumor cell lines

Tumor antigen-encoding pMFG-Cerulean or EGFP vectors

pMFG-$OVA_{257-264}$-Cerulean, pMFG-$GP_{61–80}$-Cerulean, and pMFG-$OVA_{257-264}$-$GP_{61–80}$-Ceruelan (and similar EGFP plasmids) were constructed by inserting annealed oligonucleotides encoding triple SIINFEKL-AAY repeats, GLKGPDIYKGVYQFKSVEFD, or (SIINFEKL-AAY)3-P2A-GLKGPDIYKGVYQFKSVEFD, respectively, into the NcoI-linearized pMFG-Cerulean or pMFG-EGFP vectors, as previously described.[46] Restriction enzymes were purchased from New England Biolabs. All constructs were verified by sequence analysis. Phoenix packaging cells (ATCC) were transfected with pMFG constructs; supernatants were used to transduce B16 mouse melanoma tumor cell line to generate B16 $OVA_{257-264}$-Cerulean/EGFP, B16 GP_{61-80}-Cerulean/EGFP and B16 $OVA_{257-264}$-GP_{61-80}-Cerulean/EGFP, respectively.[46] Transduced bulk cell lines were sorted for similar Cerulean or EGFP expression levels. Similar approach was used for MCA 205 fibrosarcoma cell line.

B16 and MCA205 transplantation tumor models

$2.5x10^6$ B16 $OVA_{257-264}$-GP_{61-80} (B16-OG) tumor cells, or a mixture of $1.25x10^6$ B16 $OVA_{257-264}$ (B16-O) + $1.25x10^6$ B16 GP_{61-80} (B16-G) tumor cells (B16 O+G), or MCA $OVA_{257-264}$-GP_{61-80} (MCA-OG) tumor cells were injected subcutaneously into mice. Antigen-specific T cells were adoptively transferred into tumor-bearing mice as described in text and figure legends. For outgrowth experiments, tumors were measured manually with a caliper. Tumor volume was estimated with the formula (L x W x H)/2.

Flow cytometric analysis

Flow cytometric analysis was performed using Fortessa X20. Cells were sorted using BD FACS Aria (BD Biosciences) at the MSKCC Flow Core Facility. Flow data were analyzed with FlowJo v.10 software (Tree Star Inc.).

Intracellular cytokine staining

Intracellular cytokine staining was performed using the Foxp3 staining kit (BD Biosciences) following the manufacturer's protocol. Briefly, T cells isolated from lymph nodes or tumors were mixed with $3x10^6$ congenically marked B6 splenocytes and incubated with 1 μg/mL of OVA peptide and/or 2 μg/mL of GP peptide for 4-5h at 37°C in the presence of GolgiPlug (BD Biosciences). After staining for cell surface molecules, cells were fixed, permeabilized and stained with antibodies against IFNγ (XMG1.2) and TNFα (MP6-XT22).

In vitro T cell activation

For the generation of effector TCR_{OT1} $CD8^+$ T cells and TCR_{SMARTA} $CD4^+$ T cells, single-cell suspensions were prepared from spleens of TCR_{OT1} and TCR_{SMARTA} transgenic mice and cultured *in vitro* in RPMI 1640 medium supplemented with 10% FBS, 100 IU/mL penicillin, 100 mg/mL streptomycin, nonessential amino acids, 1 mM sodium pyruvate, and 20 mM HEPES, together with 1 μg/mL of $OVA_{257-264}$ peptide or 2 μg/mL of $GP_{61–80}$ peptide, respectively, at a concentration of $4-5x10^6$ splenocytes/ml in the presence of 50U/mL IL-2 for 4 days.

Adoptive T cell transfer

For adoptive transfer studies, $2.5x10^5$ *in vitro* activated TCR_{OT1} (CD45.1) and/or $5x10^5$ *in vitro* activated TCR_{SMARTA} (Thy1.1) were transferred (i.v.) into tumor-bearing WT B6 mice at indicated time points post tumor transplantation (approximately 2–3 weeks post tumor implantation). Tumor-bearing mice were treated with cyclophosphamide (200 mg/kg), and 24h later *in vitro* activated TCR_{OT1} $CD8^+$ T cells and/or TCR_{SMARTA} $CD4^+$ T cells were adoptively transferred. At indicated time points, adoptively transferred T cells were isolated from tumor-draining lymph nodes and tumors and prepared for downstream analyses.

Anti-PD-1 and anti-PD-L1 treatment

Tumor-bearing mice were treated with anti-PD-1 and anti-PD-L1 monoclonal antibodies (20 μg (i.p.) each, per mouse). Antibodies were obtained from BioXCell; InVivoMAb anti-mouse PD-1 (CD279) Cat# BE0146; InVivoMAb anti-mouse PD-L1 (B7-H1) Cat#BE0101.

Generation of bone marrow chimeras and depletion of dendritic cells *in vivo*

B6 WT (CD45.1) mice were irradiated twice with 600 cGy, 6 h apart. 12–18 h later, bone marrow (BM) was isolated from femurs and tibias of CD11c-DTR/GFP (CD45.2) mice, and 5–8x10^6 BM cells were injected i.v. into irradiated CD45.1 mice. BM chimeric were given antibiotics (trimethoprim-sulfamethoxazole) for 2 weeks. BM chimeric were analyzed for successful engraftment and BM reconstitution 6–8 weeks later. For conditional DC depletion, CD11c-DTR/GFP BM chimeric mice were injected (i.p.) with 4–5 ng/g body weight diphtheria toxin (DT, Sigma-Aldrich) every other day for 14 days.

Generation of B16 *I-A^b*-deficient tumor cell line

The B16 tumor cells were subjected to CRISPR/Cas9-mediated knockout of *I-A^b* by transient transfection of a plasmid encoding both Cas9 nuclease and single guide (sg) RNA targeting the *I-A^b* locus, as well as GFP reporter gene. 2.5x10^5 B16 cells were plated and transfected with 2μg of Cas9-and sgRNA-encoding plasmid DNA using Lipofectamine 3,000 (Invitrogen) following the manufacturer's protocol. 3 days post transduction, GFP$^+$ cells were FACS-sorted. Deletion of *I-A^b* was confirmed by treating GFP$^+$ B16 *I-A$^{b\text{-}edited}$* cells with 20 U/ml IFNγ for 48h, followed by flow cytometric analysis of I-A^b expression.

Color-coded tumor model and adoptive transfer of color-coded T cells

CD11c-YFP transgenic mice were injected subcutaneously with 2.5x10^6 (B16-OG) tumor cells or a mixture of 1.25x10^6 B16-O + 1.25x10^6 B16-G tumor cells (B16 O+G). To generate color coded TCR_{OT1} CD8$^+$ T cells, TCR_{OT1} splenocytes were transduced to express tRFP using retroviral transduction as previously described.[78] Briefly, Platinum-E cells were transfected with a tRFP-encoding retroviral vector using the Mirus TransIT-LT1 reagent (catalog no. 2305). Viral supernatant was supplemented with polybrene and added to TCR_{OT1} splenocytes, and the cells were transduced via spinfection on two consecutive days. To generate color-coded TCR_{SMARTA} CD4$^+$ T cells, splenocytes from TCR_{SMARTA} GFP transgenic mice were used and activated as described above. Tumor-bearing mice were treated with cyclophosphamide (180 mg/kg) one day before ACT, and *in vitro* activated 2.5 + 10^5 TCR_{OT1} tRFP$^+$ CD8$^+$ T cells and 4X10^5 cells TCR_{SMARTA} EGFP CD4$^+$ T cells were transferred (i.v.) into tumor-bearing mice.

Immunofluorescence staining and confocal imaging

For confocal microscopy analysis, pieces of established tumors were excised and fixed for 18–24 h in 4% paraformaldehyde solution, followed by dehydration in 20% sucrose, and then embedded in OCT, and stored at −80°C. 30-μm-thick frozen sections were cut on a CM3050S cryostat (Leica) and adhered to Superfrost Plus slides (Thermo Fisher Scientific). Nuclei were labeled using DAPI (Sigma). Slides were mounted with ProLong Diamond Antifade Mountant (Invitrogen) and analyzed on a Leica TCS SP8 confocal microscope. Fiji Is Just ImageJ (FIJI) was utilized for image analysis. 3D reconstitution was performed, and triple contacts/triads were assessed based on color-coded immune subset identification. Analyses was performed as a blinded outcome assessment. To quantify double contacts, after thresholding and binarization of images, the function "analyze particles" has been applied. To precisely estimate only events showing double contact, the mathematical function "AND" was used.

Isolation of adoptively transferred T cells from downstream analyses

Lymph nodes were mechanically disrupted with the back of a 3-mL syringe, filtered through a 100-μm strainer, and red blood cells (RBC) were lysed with ammonium chloride potassium buffer. Cells were washed twice with cold RPMI 1640 media supplemented with 2μM glutamine, 100U/mL penicillin/streptomycin, and 3% fetal bovine serum (FBS). Tumor tissue was mechanically disrupted with a glass pestle and a 150-μm metal mesh in 5mL of cold HBSS with 3% FBS. Cell suspension was filtered through 70-μm strainers. Tumor homogenate was spun down at 400*g* for 5 min at 4°C. Pellet was resuspended in 15 mL HBSS with 3% FBS, 500 μL (500U) heparin, and 8 mL isotonic Percoll (GE), mixed by several inversions, and spun at 500*g* for 10 min at 4°C. Pellet was lysed with ammonium chloride potassium buffer and cells were further processed for downstream applications.

Sample preparation for RNA-Seq and ATAC-Seq

TCR_{OT1} CD8$^+$ T cells were isolated from tumors (see above); cells were stained for CD8α (clone 53–6.7, eBioscience) and CD45.1$^+$ (clone A20, Biolegend). CD8$^+$ CD45.1$^+$ cells were sorted by FACS. For RNA-seq, T cells were directly sorted into Trizol LS reagent (Invitrogen, catalog no. 10296010) and stored at −80°C. For ATAC-seq, sorted T cells were resuspended in cold FBS with 10% DMSO and stored at −80°C.

RNA-seq

RNA from sorted cells was extracted using the RNeasy Mini Kit (Qiagen; catalog no. 74104) according to instructions provided by the manufacturer. After RiboGreen quantification and quality control by an Agilent BioAnalyzer, total RNA underwent amplification using the SMART-Seq v4 Ultra Low Input RNA Kit (Clontech), and amplified cDNA was used to prepare libraries with the KAPA Hyper Prep

Kit (Kapa Biosystems). Samples were barcoded and run on a HiSeq 2500 in a 50-bp/50-bp paired-end run with the HiSeq SBS Kit v4 (Illumina). An average of 50 million paired reads were generated per sample.

ATAC-seq

Profiling of chromatin accessibility was performed by ATAC-seq as previously described (Buenrostro et al., 2013). Briefly, viably frozen, sorted T cells were washed in cold PBS and lysed. The transposition reaction was incubated at 42°C for 45 min. The DNA was cleaned with the MinElute PCR Purification Kit (Qiagen; catalog no. 28004), and material was amplified for five cycles. After evaluation by real-time PCR, 7–13 additional PCR cycles were done. The final product was cleaned by AMPure XP beads (Beckman Coulter, catalog no. A63882) at a 1× ratio, and size selection was performed at a 0.5× ratio. Libraries were sequenced on a HiSeq 2500 or HiSeq 4000 in a 50-bp/50-bp paired-end run using the TruSeq SBS Kit v4, HiSeq Rapid SBS Kit v2, or HiSeq 3000/4000 SBS Kit (Illumina). An average of 100 million paired reads were generated per sample.

Bioinformatics methods

The quality of the sequenced reads was assessed with FastQC and QoRTs (for RNA-seq samples; Hartley and Mullikin, 2015; Andrews, 2010). Unless stated otherwise, plots involving high-throughput sequencing data were created using R version 4.1.0 (R Core Team, 2017) and ggplot2 (Wickham, 2016).

RNA-seq data

DNA sequencing reads were aligned with default parameters to the mouse reference genome (GRCm38.p6) using STAR v2.6.0c (Dobin et al., 2013).[79] Gene expression estimates were obtained with featureCounts v1.6.2 using composite gene models (union of the exons of all transcript isoforms per gene) from Gencode (version M17; Liao et al., 2014).[80]

Differentially expressed genes

DEGs were determined using DESeq2 v1.34.0 with Wald tests with a q-value cutoff of 0.05 (Benjamini–Hochberg correction).[81]

Heatmaps

Heatmaps were created using DESeq2 normalized read counts after variance stabilizing transformation of genes identified as differentially expressed by DESeq2. Rows were centered and scaled.

Pathway and GO term enrichment analyses

Gene set enrichment analyses were done using fgsea v1.20.0[82] with the fgseaMultilevel function. Genes were ranked based on the DESeq2 Wald statistic. Gene sets with an FDR <0.05 were considered enriched.

Gene ontology analysis was performed on up- and down-regulated DEGs using the clusterProfiler v4.2.2 R package.[94,83] Only GO categories enriched using a 0.05 false discovery rate cutoff were considered.

ATAC-seq data

Alignment and creation of peak atlas

Reads were aligned to the mouse reference genome (version GRCm38) with BWA-backtrack v0.7.17.[84] Post-alignment filtering was done with samtools v1.8[85] and Picard tools v2.18.9 to remove unmapped reads, improperly paired reads, nonunique reads, and duplicates. Peaks were called with MACS2 v2.1.1,[86] and peaks with adjusted *p* values smaller than 0.01 were excluded. Consensus peak sets were generated for each condition if a peak was found in at least two replicates. Reproducible peaks from each condition were merged with DiffBind v3.4.11 to create an atlas of accessible peaks, which was used for downstream analyses. The peak atlas was annotated using the ChIPseeker v1.30.3[95,88] and TxDb.Mmusculus.UCSC.mm10.knownGene [Bioconductor Core Team and Bioconductor Package Maintainer (2019). TxDb.Mmusculus.UCSC.mm10.knownGene: Annotation package for TxDb object(s). R package version 3.10.0.]. Blacklisted regions were excluded (https://sites.google.com/site/anshulkundaje/projects/blacklists).

Differentially accessible regions

Regions where the chromatin accessibility changed between different conditions were identified with DESeq2 v1.34.0, and only Benjamini–Hochberg corrected *p* values <0.05 were considered statistically significant.

Coverage files

Genome coverage files were normalized for differences in sequencing depth (RPGC normalization) with bamCoverage from deepTools v3.1.0.[89] Replicates were averaged together using UCSC-tools bigWigMerge.[90]

Heatmaps

Heatmaps based on the differentially accessible peaks identified between TCR_{OT1} and $TCR_{OT1}^{(+CD4)}$ were created using profileplyr v1.10.2 (T. Carroll and D. Barrows (2021)). profileplyr: Visualization and annotation of read signal over genomic ranges with profileplyr. R package version 1.10.2.) and ComplexHeatmap v2.15.1,[96] by binning the region +/− 1kb around the peak summits in 20bp bins. To improve visibility, bins with read counts greater than the 75th percentile +1.5*IQR were capped at that value.

Motif analyses

For identifying motifs enriched in differentially accessible peaks, we utilized HOMER via marge v0.0.4[93] [Robert A. Amezquita (2021). marge: API for HOMER in R for Genomic Analysis using Tidy Conventions. R package version 0.0.4.9999]. HOMER was run separately on hyper- or hypo-accessible peaks with the flags -size given and -mask. Motifs enriched in hyper- or hypo-accessible peaks were determined by comparing the rank differences (based on *p* value). The consensus peakset identified by DiffBind was used as the background set.

Human samples analyses

Cancer specimens were processed into single-cell suspensions, fresh frozen tissue preparations, samples cryopreserved in optimal cutting temperature (OCT) compound, and formaldehyde-fixed paraffin-embedded tissues (FFPE).

Imaging mass cytometry (IMC). FFPE tissue samples were sectioned at a 5-μm thickness for IMC. FFPE tissues on charged slides were stained with 1:100 diluted antibody cocktails (concentration of each antibody = 0.5 mg/mL) as recommended by the user's manual. The slides were scanned in the Hyperion Imaging System (Standard BioTools). They were scanned at least four regions of interest in >1mm^2 at 200 Hz.

IMC analysis. Fiji was used for cell segmentation and conversion of imaging data into flow cytometric data, with the advantage of fast, robust, unsupervised, automated cell segmentation method. 32-bit TIFF stacked images were loaded in Fiji and novel method of automated cell segmentation that estimates cell boundaries by expanding the perimeter of their nuclei, identified by Cell ID intercalator iridium (191Ir) was used as described in more detail.[69] Once images from the IMC methodology were acquired, images were quantified through FIJI's threshold and watershed tools. Protein expression data were then extracted at the single-cell level through mean intensity multiparametric measurements performed on individual 10 cells and acquired single-cell data were transferred into additional cytometric analysis in FlowJo V10 software (FlowJo, LLC, OR). All protein markers in quantified IMC data are adjusted with 191Ir and 193Ir nucleus intensities and normalized with CytoNorm across IMC regions of interests, a normalization method for cytometry data applicable to large clinical studies that is plugged-in FlowJo. CytoNorm allows reducing mass cytometry signal variability across multiple batches of barcoded samples. Normalized IMC data are combined by using FlowJo.

Characterization of cell phenotypes and cell density analysis. For cellular phenotype characterization and cell density analysis, raw data, stored as.mcd files, were transformed into TIFF format using a specialized Python package adapted from the Elemento Lab IMC Python Package (https://github.com/ElementoLab/imc). These TIFF files were further analyzed with the Ilastik tool to predict cellular locations and boundaries via pixel and object classification.[97] Single-cell segmentation for each image was achieved using the DeepCell package.[98,99] Nuclear analysis was integrated with cell boundary data to determine cell segmentation. The mean expressions of panels from segmented single cells were retrieved using the IMC package by overlaying segmentation masks onto the corresponding TIFF images. Resulting segmented images and data files were cataloged into CSV and AnnData formats. For enhanced precision in cell protein expression metrics, we employed the PowerTransform (Yeo-Johnson) normalization tools designed for skewed and bimodal condition interpretations. This normalization was executed for each region of interest and individual sample. To compare the characteristics of cellular phenotypes, $CD4^+$ or $CD8^+$ T cells were isolated from triads, dyads, or regions devoid of these structures. To explore cell-cell interactions, we employed a permutation test approach available in the SCANPY and SCIMAP packages.[100] This method determines if interactions or avoidances within or between cell types surpass random occurrence frequencies. The IMC images were transposed into topological neighborhood graphs, wherein cells were depicted as nodes. Direct cell-cell neighboring pairs, within a 100-400μm range between centroids, were depicted as edges. The quantification of neighborhoods is predicated upon the cellular density surrounding the center of triad or dyad, facilitating comparisons between grouped datasets.

QUANTIFICATION AND STATISTICAL ANALYSIS

Details of the statistical analyses performed on each experiment are indicated in the respective figure legends. For flow cytometric data analyses unpaired two-tailed Student's *t* tests or other statistical testing methods were used as described in figure legends; for tumor growth curves significance was calculated by two-way ANOVA with Bonferroni correction. The data are presented as mean ± SEM. All *p*-values<0.05 were considered statistically significant. Mice were randomized before grouping.